Mon. Not. R. Astron. Soc. **382,** 251–269 (2007) doi:10.1111/j.1365-2966.2007.12351.x

The metal abundance of circumnuclear star-forming regions in early-type spirals. Spectrophotometric observations

Ángeles I. Díaz,[1]★† Elena Terlevich,[2]‡ Marcelo Castellanos[1]§ and Guillermo F. Hägele[1]¶

[1]*Departamento de Física Teórica, C-XI, Universidad Autónoma de Madrid, 28049 Madrid, Spain*
[2]*INAOE, Tonantzintla, Apdo. Postal 51, 72000 Puebla, México*

Accepted 2007 August 8. Received 2007 July 19; in original form 2007 June 8

ABSTRACT

We have obtained long-slit observations in the optical and near-infrared of 12 circumnuclear H II regions [circumnuclear star-forming regions (CNSFR)] in the early-type spiral galaxies NGC 2903, 3351 and 3504 with the aim of deriving their chemical abundances. Only for one of the regions, the [S III] λ6312 Å was detected providing, together with the nebular [S III] lines at λλ9069, 9532 Å, a value of the electron temperature of $T_e([S\,III]) = 8400^{+4650}_{-1250}$ K. A semi-empirical method for the derivation of abundances in the high metallicity regime is presented.

We obtain abundances which are comparable to those found in high metallicity disc H II regions from direct measurements of electron temperatures and consistent with solar values within the errors. The region with the highest oxygen abundance is R3+R4 in NGC 3504, $12 + \log(O/H) = 8.85$, about 1.5 solar if the solar oxygen abundance is set at the value derived by Asplund, Grevesse & Sauval, $12 + \log(O/H)_\odot = 8.66 \pm 0.05$. Region R7 in NGC 3351 has the lowest oxygen abundance of the sample, about 0.6 times solar. In all the observed CNSFR the O/H abundance is dominated by the O^+/H^+ contribution, as is also the case for high metallicity disc H II regions. For our observed regions, however, also the S^+/S^{2+} ratio is larger than one, contrary to what is found in high metallicity disc H II regions for which, in general, the sulphur abundances are dominated by S^{2+}/H^+.

The derived N/O ratios are in average larger than those found in high metallicity disc H II regions and they do not seem to follow the trend of N/O versus O/H which marks the secondary behaviour of nitrogen. On the other hand, the S/O ratios span a very narrow range between 0.6 and 0.8 of the solar value.

As compared to high metallicity disc H II regions, CNSFR show values of the O_{23} and the N2 parameters whose distributions are shifted to lower and higher values, respectively, hence, even though their derived oxygen and sulphur abundances are similar, higher values would in principle be obtained for the CNSFR if pure empirical methods were used to estimate abundances. CNSFR also show lower ionization parameters than their disc counterparts, as derived from the [S II]/[S III]. Their ionization structure also seems to be different with CNSFR showing radiation field properties more similar to H II galaxies than to disc high metallicity H II regions.

Key words: ISM: abundances – H II regions – galaxies: abundances.

1 INTRODUCTION

The inner (∼1 kpc) parts of some spiral galaxies show high star formation rates and this star formation is frequently arranged in a ring or pseudo-ring pattern around their nuclei. This fact seems to correlate with the presence of bars and, in fact, computer models which simulate the behaviour of gas in galactic potentials have shown that

★E-mail: angeles.diaz@uam.es
†On sabbatical leave at IoA, Cambridge.
‡Research Affiliate at IoA.
§At present at the Intituto de Estructura de la Materia, CSIC, Spain.
¶PhD fellow of Ministerio de Educación y Ciencia, Spain.

nuclear rings may appear as a consequence of matter infall owing to resonances present at the bar edges (Combes & Gerin 1985; Athanassoula 1992).

In general, circumnuclear star-forming regions (CNSFR), also referred to as 'hotspots', and luminous and large disc H II regions are very much alike, but look more compact and show higher peak surface brightness (Kennicutt, Keel & Blaha 1989). In many cases they contribute substantially to the emission of the entire nuclear region.

Their large Hα luminosities, typically higher than 10^{39} erg s^{-1}, point to relatively massive star clusters as their ionization source, which minimizes the uncertainties due to small number statistics when applying population synthesis techniques (see e.g. Cerviño et al. 2002). These regions then constitute excellent places to study how star formation proceeds in high metallicity, high density circumnuclear environments.

In many cases, CNSFR show emission-line spectra similar to those of disc H II regions. However, they show a higher continuum from background stellar populations as expected from their circumnuclear location, often inside 500 pc from the galaxy centre. In early-type spirals CNSFR are also expected to be amongst the highest metallicity regions as corresponds to their position near the galactic bulge. These facts taken together make the analysis of these regions complicated since, in general, their low excitation makes any temperature sensitive line too weak to be measured, particularly against a strong underlying stellar continuum. In fact, in most cases, the [O III]λ5007 Å line, which is typically 100 times more intense than the auroral [O III]λ4363 Å one, can be barely seen.

Yet, despite its difficulty, the importance of an accurate determination of the abundances of high metallicity H II regions cannot be overestimated since they constitute most of the H II regions in early spiral galaxies (Sa to Sbc) and the inner regions of most late-type ones (Sc to Sd) (Díaz 1989; Vila-Costas & Edmunds 1992) without which our description of the metallicity distribution in galaxies cannot be complete. In particular, the effects of the choice of different calibrations on the derivation of abundance gradients can be very important since any abundance profile fit will be strongly biased towards data points at the ends of the distribution. It should be kept in mind that abundance gradients are widely used to constrain chemical evolution models, histories of star formation over galactic discs or galaxy formation scenarios. The question of how high is the highest oxygen abundance in the gaseous phase of galaxies is still standing and extrapolation of known radial abundance gradients would point to CNSFR as the most probable sites for these high metallicities.

Accurate measures of elemental abundances of high metallicity regions are crucial to obtain reliable calibrations of empirical abundance estimators, widely used but poorly constrained, whose choice can severely bias results obtained for quantities of the highest relevance for the study of galactic evolution like the luminosity–metallicity (L–Z) relation for galaxies. CNSFR are also ideal cases to study the behaviour of abundance estimators in the high metallicity regime.

In Section 2 of this paper we describe the sample of regions observed and the circumnuclear environment of their host galaxies. Our observations and the data reduction procedures are described in Section 3. The results are presented in Section 4. The method for the derivation of chemical abundances is described in Section 5. Section 6 is devoted to the discussion of our results. Finally, Section 7 summarizes the main conclusions of this work.

Table 1. The galaxy sample.

Property	NGC 2903	NGC 3351	NGC 3504
RA (2000)[a]	09 32 10.1	10 43 57.7	11 03 11.2
Dec. (2000)[a]	+21 30 03	+11 42 14	+27 58 21
Morph. type	SBbc	SBb	SABab
Distance (Mpc)[b]	8.6	10	20
pc/arcsec	42	50	100
B_T (mag)[a]	9.7	10.5	11.8
$E(B-V)_{gal}$ (mag)[a]	0.031	0.028	0.027

[a]de Vaucouleurs et al. (1991).
[b]NGC 2903: Bottinelli et al. (1984);
NGC 3351: Graham et al. (1997);
NGC 3504: Kenney et al. (1992).

2 SAMPLE SELECTION

We have obtained moderate resolution observations of 12 CNSFR in three 'hotspot' galaxies: NGC 2903, 3351 and 3504 whose main properties are given in Table 1. The three of them are early barred spirals and show a high star formation rate in their nuclear regions. They are quoted in the literature as among the spirals with the highest overall oxygen abundances (Zaritsky, Kennicutt & Huchra 1994; Pérez-Olea 1996).

NGC 2903 is a well-studied galaxy. The Paschen α image obtained with the *Hubble Space Telescope* (*HST*) reveals the presence of a nuclear ring-like morphology with an apparent diameter of approximately 15 arcsec = 625 pc (Alonso-Herrero, Ryder & Knapen 2001). This structure is also seen, though less prominent, in the Hα observations from Planesas, Colina & Perez-Olea (1997). A large number of stellar clusters are identified on high-resolution infrared images in the K' and H bands, which do not coincide spatially with the bright H II regions. A possible interpretation of this is that the stellar clusters are the result of the evolution of giant H II regions (e.g. Alonso-Herrero et al. 2001). The global star formation rates in the nuclear ring, as derived from its Hα luminosity is found to be 0.1 M$_\odot$ yr^{-1} by Planesas et al. (1997) and 0.7 M$_\odot$ yr^{-1} from Alonso-Herrero et al. (2001). From CO emission observations, Planesas et al. (1997) derive a mass of molecular gas (H_2) of 1.8×10^8 M$_\odot$ inside a circle 1 kpc in diameter.

NGC 3351 is another well known 'hotspot' galaxy (Sérsic & Pastoriza 1967). Early detailed studies of its nuclear regions (Alloin & Nieto 1982) concluded that NGC 3351 harbours high-mass circumnuclear star formation. In fact, the star formation rate per unit area in the nuclear region is significantly increased over that observed in the disc (Devereux, Kenney & Young 1992). Elmegreen et al. (1997) from near-infrared (IR) photometry in the J and K bands derive a circumnuclear star formation rate of 0.38 M$_\odot$ yr^{-1}. Planesas et al. (1997), from the Hα emission, derive a total star formation rate for the circumnuclear region of 0.24 M$_\odot$ yr^{-1} and a mass of molecular gas of 3.5×10^8 M$_\odot$ inside a circle of 1.4 kpc in diameter, from CO emission observations. A recent kinematical study of the CNSFR has been presented in Hägele et al. (2007a).

NGC 3504 is the brightest galaxy in the optically selected catalogue of starburst galactic nuclei in Balzano (1983). It forms a pair with NGC 3512. Various studies at different wavelengths confirmed that it harbours a very intense nuclear starburst (Devereux 1989; Puxley, Hawarden & Mountain 1990). Infrared observations in the J and K bands reveal a ring with five discrete clumps of star formation with colours indicating ages of about 10^7 yr (Elmegreen et al. 1997). The Hα emission from Planesas et al. (1997) traces a

Table 2. Journal of observations.

Galaxy	Spectral range (Å)	Grating	Disp. (Å pixel^{-1})	Spatial resolution (arcsec pixel^{-1})	PA (°)	Exposure time (s)
NGC 2903	3650–7000	R300B	1.73	0.4	105	2×1800
NGC 2903	8850–9650	R600R	0.79	0.4	105	2×1800
NGC 2903	3650–7000	R300B	1.73	0.4	162	2×1800
NGC 2903	8850–9650	R600R	0.79	0.4	162	2×1800
NGC 3351	3650–7000	R300B	1.73	0.4	10	2×1800
NGC 3351	8850–9650	R600R	0.79	0.4	10	2×1800
NGC 3351	3650–7000	R300B	1.73	0.4	38	2×1800
NGC 3351	8850–9650	R600R	0.79	0.4	38	2×1800
NGC 3351	3650–7000	R300B	1.73	0.4	61	2×1800
NGC 3351	8850–9650	R600R	0.79	0.4	61	2×1800
NGC 3504	3650–7000	R300B	1.73	0.4	110	2×1800
NGC 3504	8850–9650	R600R	0.79	0.4	110	2×1800

compact ring structure with a radius of 2 arcsec (200 pc) around the nucleus where four separated H II regions can be identified. From the Hα emission, these authors derive a global star formation rate for the circumnuclear region of 0.62 $M_\odot$ yr^{-1}, while from their CO observations, a molecular gas mass of 21×10^8 $M_\odot$ inside a circle 2.7 kpc in diameter is derived.

3 OBSERVATIONS AND DATA REDUCTION

Our spectrophotometric observations were obtained with the 4.2-m William Herschel Telescope (WHT) at the Roque de los Muchachos Observatory, in 2001 January 26, using the ISIS (Integrated Science Instrument Server) double spectrograph, with the EEV12 and TEK4 detectors in the blue and red arm, respectively. The incoming light was split by the dichroic at λ7500 Å. Gratings R300B in the blue arm and R600R in the red arm were used, covering 3400 Å in the blue (λ3650 to λ7000) and 800 Å in the near-IR (λ8850 to λ9650) and yielding spectral dispersions of 1.73 Å pixel^{-1} in the blue arm and 0.79 Å pixel^{-1} in the red arm. With a slitwidth of 1.05 arcsec, spectral resolutions of ∼2.0 and 1.5 Å FWHM (full width at half-maximum) in the blue and red arms, respectively, were attained. This is an optimal configuration which allows the simultaneous observation of a given region in both frames in a single exposure.

The nominal spatial sampling is 0.4 arcsec pixel^{-1} in each frame and the average seeing for this night was ∼1.2 arcsec. A journal of the observations is given in Table 2.

Two, three and one slit positions in NGC 2903, 3551 and 3504, respectively, were chosen to observe a total of 12 CNSFR. Fig. 1 shows the different slit positions superimposed on images obtained with the *HST* Wide-Field Planetary Camera 2 (WFPC2) camera and taken from the *HST* archive. Some characteristics of the observed regions, as given by Planesas et al. (1997), from where the identification numbers have also been taken, are listed in Table 3.

The data were reduced using the Image Reduction and Analysis Facility (IRAF)[1] package following standard methods. The two-dimensional wavelength calibration was accurate to 1 Å in all cases by means of Cu, Ne and Ar calibration lamps. The two-dimensional frames were flux calibrated using four spectroscopic standard stars: Feige 34, BD 26+2606, HZ 44 and HD 84937, observed before and after each programme object with a 3 arcsec width slit. For two of the standard stars: Feige 34 and HZ 44, the fluxes have been obtained from the most updated version of the original Oke's spectra (Oke 1990) and cover the 3200 to 9200 Å range. Data between 9200 and 9650 Å have been obtained from stellar atmosphere models. For the other two stars: BD 26+2606 and HD 84937, the fluxes have been taken from Oke & Gunn (1983) that cover the whole spectral range. The agreement between the individual calibration curves was better than 5 per cent in all cases and a weighted mean calibration curve was derived. The spectra were previously corrected for atmospheric extinction using a mean extinction curve applicable to La Palma observing site.

Regarding background subtraction, the high spectral dispersion used in the near-IR allowed the almost complete elimination of the night-sky OH emission lines and, in fact, the observed λ9532/λ9069 ratio is close to the theoretical value of 2.44 in most cases. Telluric absorptions have been removed from the spectra of the regions by dividing by the relatively featureless continuum of a subdwarf star observed in the same night.

4 RESULTS

Fig. 2 shows the spatial distribution of the Hα flux along the slit for the six different positions observed in the sample, a single one in the case of NGC 3504, two in NGC 2903 and three in NGC 3351. The regions that were extracted into one-dimensional spectra are delimited by arrows. The spectra corresponding to each of the identified regions are shown in Figs 3, 4 and 5 for NGC 2903, 3351 and 3504, respectively.

4.1 Underlying population

The presence of underlying Balmer stellar absorptions is clearly evident in the blue spectra of the observed regions (see Figs 3, 4 and 5) and complicates the measurements. A two-component – emission and absorption – Gaussian fit was performed in order to correct the Balmer emission lines for this effect. An example of this procedure can be seen in Fig. 6. The equivalent widths (in Åmstrongs) of the Gaussian absorption components resulting from the fits are given in Table 4 together with the ratio between the line flux measured after subtraction of the absorption component and the line flux measured without any correction and using a pseudo-continuum placed at the bottom of the line. This factor provides a

[1] IRAF: the Image Reduction and Analysis Facility is distributed by the National Optical Astronomy Observatories, which is operated by the Association of Universities for Research in Astronomy, Inc. (AURA) under cooperative agreement with the National Science Foundation (NSF).

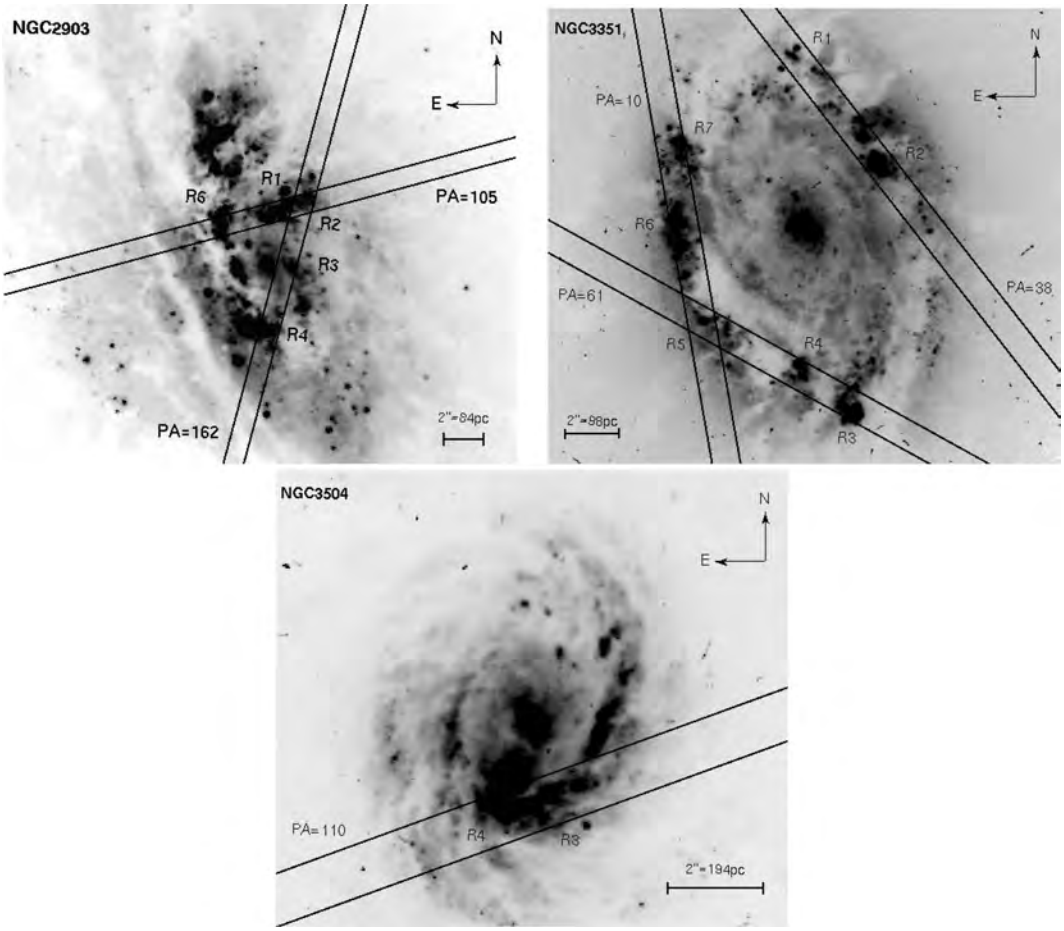

Figure 1. Observed CNSFR in each of the galaxies. The different slit positions are superimposed on images taken from the *HST* archive and obtained with the WFPC2 camera through the F606W filter. The position angles (PAs) of every slit position are indicated.

Table 3. Characteristics of the CNSFR observed.

Galaxy	Region	Offsets from centre (arcsec)	Diameter[a] (arcsec)	$F(\mathrm{H}\alpha)$ ($\times 10^{-14}$ erg s^{-1} cm^{-2})
NGC 2903	R1+R2	−1.7, +3.5	4.0	22.8
	R3	−1.6, −0.3	2.0	2.6
	R4	−0.3, −3.3	2.4	10.1
	R6	+2.3, +2.4	2.4	12.7
NGC 3351	R1	+0.4, +6.5	2.4	12.3
	R2	−2.6, +2.6	2.4	16.0
	R3	−1.5, −6.5	2.4	20.7
	R4	+0.5, 5.4	2.2	10.5
	R5	+2.9, −3.5	2.4	4.9
	R6	+4.1, −0.4	2.4	6.1
	R7	+4.8, +3.6	1.8	9.5
NGC 3504	R3+R4	−0.5, −1.7	1.6	21.6

[a]Size of the circular aperture used to measure fluxes.

value for the final correction to the measured fluxes in terms of each line flux. In regions R4 of NGC 2903 and R5 of NGC 3351 the Hδ line is seen only in absorption. In region R5 of NGC 3351 also Hγ is seen only in absorption. No fitting was performed for these lines, hence no correction is listed for them in Table 4. In the case of the He I and Paschen no prominent absorption line wings are observed that allow the fitting of an absorption component as it was done in the case of the Balmer lines. These lines were measured with respect to a local continuum placed at the their base, which partially corrects by underlying absorption.

4.2 Line intensity measurements

Emission-line fluxes were measured on the extracted spectra using the IRAF SPLOT software package, by integrating the line intensity over a local fitted continuum. The errors in the observed line fluxes

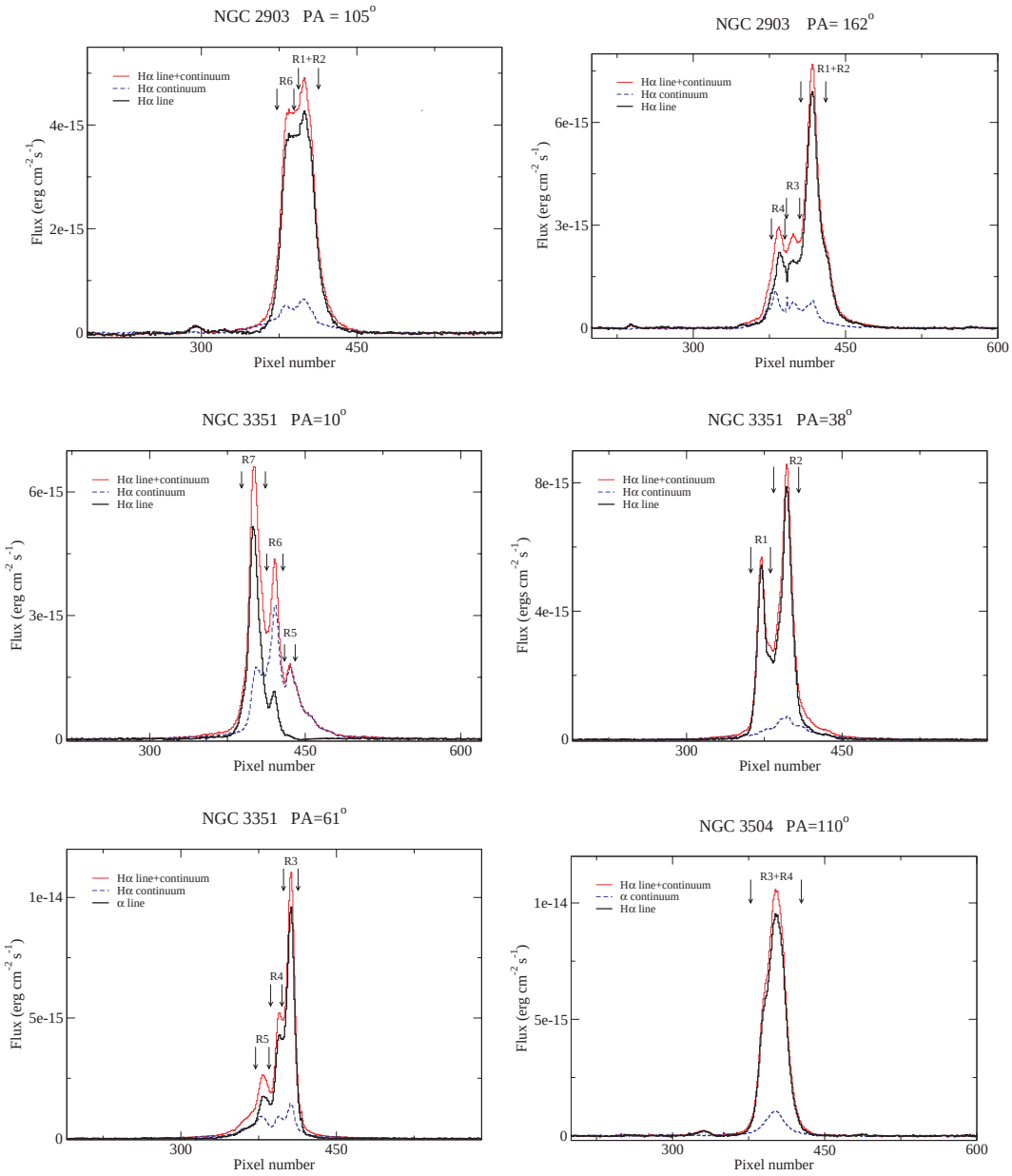

Figure 2. Hα profiles for the observed slit positions. Each figure includes the name of the galaxy and the PA of the slit, the name of the observed regions.

have been calculated from the expression $\sigma_1 = \sigma_c\, N^{1/2}\, [1 + \mathrm{EW}/(N\Delta)]^{1/2}$, where σ_1 is the error in the line flux, σ_c represents the standard deviation in a box near the measured emission line and stands for the error in the continuum placement, N is the number of pixels used in the measurement of the line flux, EW is the line equivalent width and Δ is the wavelength dispersion in Ångstroms per pixel. The first term represents the error in the line flux introduced by the uncertainty in the placement of the continuum, while the second one scales the signal-to-noise ratio in the continuum to the line (Gonzalez-Delgado et al. 1994).

The Balmer emission lines were corrected for the underlying absorption as explained above. Then the logarithmic extinction at Hβ, c(Hβ) was calculated from the Balmer line decrements assuming the Balmer line theoretical values for case B recombination (Brocklehurst 1971) for a temperature of 6000 K, as expected for high metallicity regions, and an average extinction law (Miller & Mathews 1972). An example of this procedure is shown in Fig. 7 for region R1+R2 of NGC 2903, where the logarithm of the quotient between observed and theoretical Balmer decrements is represented against the logarithmic extinction at the Balmer line wavelengths, $f(\lambda)$. The tight relation found for a baseline from the Paschen lines to Hδ can be taken as evidence of the reliability of our subtraction procedure for this region. This is also the case for most regions, although in some cases the Hγ/Hβ ratio lies above or below the reddening line, implying that the subtraction procedure is not that good for this line. This is not surprising since the presence of the *G* band and other metal features in the left wing of the line, makes the fitting less reliable than for the other Balmer lines. We have used all the available Balmer and Paschen-to-Balmer ratios, although due to the uncertainties in the emission line intensities of the higher

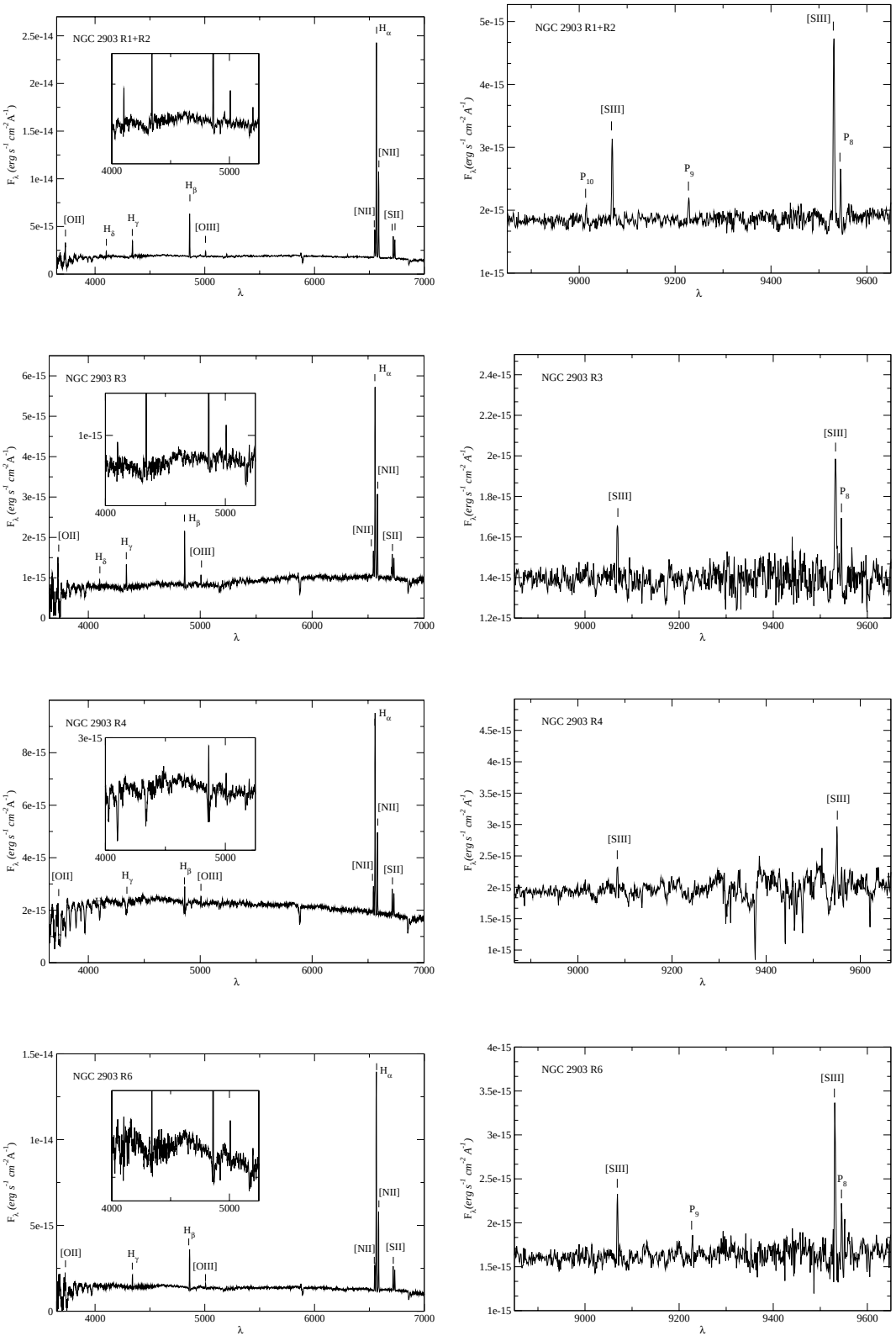

Figure 3. Extracted blue (left) and red (right) spectra for the observed regions of NGC 2903. From top to bottom: R1+R2, R3, R4 and R6.

order Balmer lines, which are difficult to estimate (in fact, in some regions they are seen only in absorption), these ratios have been given a lower weight in the fit. This almost amounts to deriving the values of $c(\mathrm{H}\beta)$ from the $\mathrm{H}\alpha/\mathrm{H}\beta$ ratio and checking for consistency against the values measured for the Paschen lines, which are much less affected by underlying absorption due the smaller contribution to the continuum from main sequence AF stars. The errors in $c(\mathrm{H}\beta)$ have in fact been derived from the measured errors in the $\mathrm{H}\alpha$ and

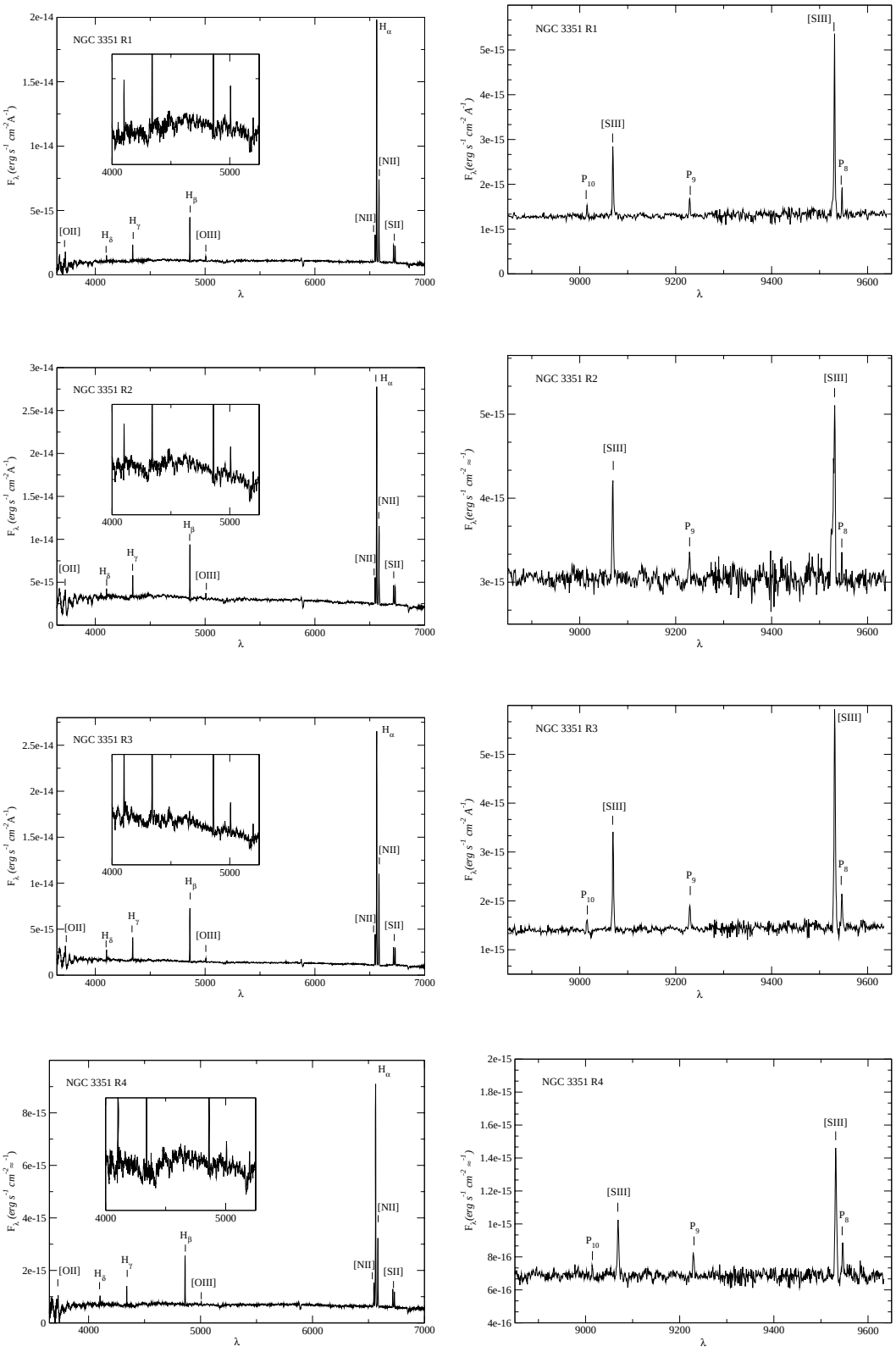

Figure 4. Extracted blue (left) and red (right) spectra for the observed regions of NGC 3351. From top to bottom: R1, R2, R3, R4, R5, R6 and R7.

Hβ lines, since in any weighted average these two lines have by far the largest weight.

The blue region of the spectrum near the Balmer discontinuity is dominated by absorption lines which cause a depression of the continuum and difficult the measurement of the [O II] lines at λ3727 Å. None of them however is at the actual wavelength of the [O II] line. This can be seen in Fig. 8 where we show the spectrum of region R1+R2 in NGC 2903 compared to that corresponding to a globular

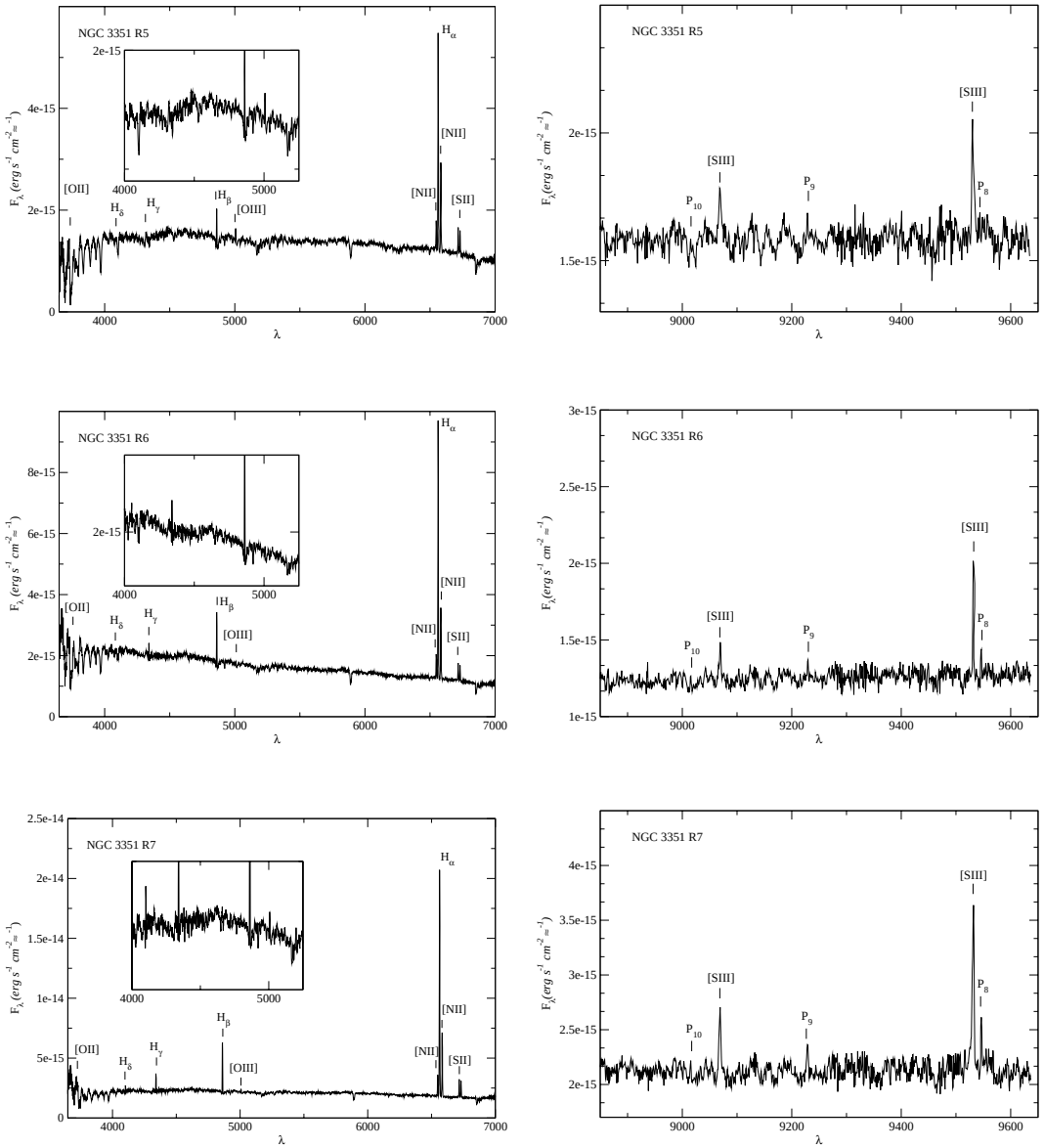

Figure 4 – *continued*

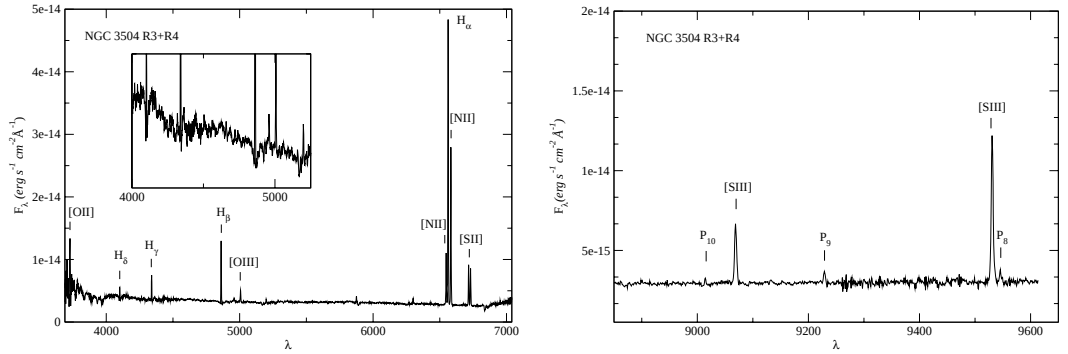

Figure 5. Extracted blue (left) and red (right) spectra for regions R3+R4 of NGC 3504.

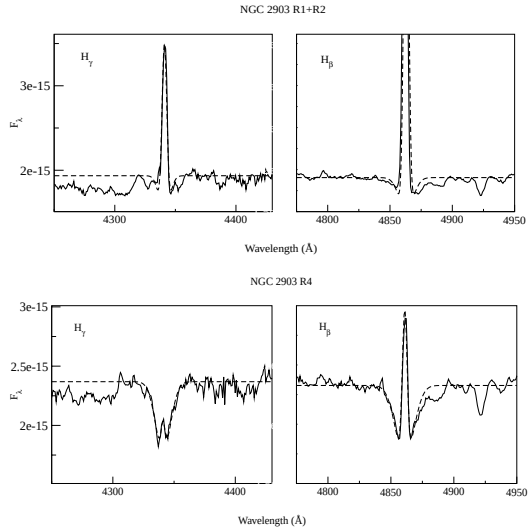

Figure 6. Examples of the fitting procedure used to correct the Balmer emission line intensities for underlying absorption.

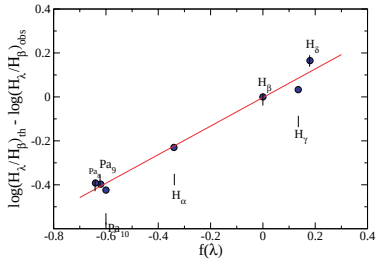

Figure 7. Reddening determination for region R1+R2 in NGC 2903. The tight relation found shows the goodness of the correction to the Balmer emission lines by the underlying absorption continuum.

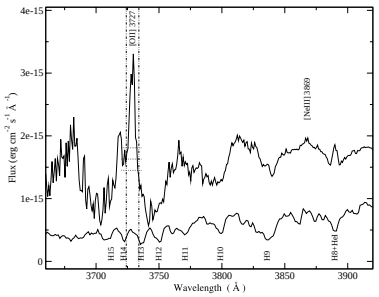

Figure 8. Blue spectrum of region R1+R2 in NGC 2903 showing the location of the [O II] λλ3727, 3729 Å lines. The spectrum below corresponds to a metal rich globular cluster in M31 which can be compared with the underlying stellar population in the region. The way in which the [O II] line has been measured by placing a local pseudo-continuum at its base is shown. The different continuum placements used for the computation of the errors are shown by horizontal lines.

cluster of M31, 337−068, of relatively high metallicity (Barmby et al. 2000; Mike Beasley, private communication). We have measured the line using a local continuum at its base as shown in the figure. The different continuum placements used for computing the error are shown by horizontal dotted lines in the figure.

Once the reddening constant was found, the measured line intensities relative to the Hβ line were corrected for interstellar reddening according to the assumed reddening law. The errors in the reddening corrected line intensities have been derived by means of error propagation theory. Measured and reddening corrected emission-line fluxes, together with their corresponding errors, are given in Tables 5, 6 and 7 for the observed CNSFR in NGC 2903, 3351 and 3504, respectively. Balmer emission lines are corrected for underlying absorption. Also given in the tables are the assumed reddening law, the Hβ intensity underlying absorption and extinction corrected, the Hβ equivalent width, also corrected for absorption, and the reddening constant.

5 CHEMICAL ABUNDANCES

Electron densities for each observed region have been derived from the [S II] λλ6717, 6731 Å line ratio, following standard methods (e.g. Osterbrock 1989). They were found to be, in all cases, $\leqslant 600\,\mathrm{cm}^{-3}$, higher than those usually derived in disc H II regions, but still below the critical value for collisional de-excitation.

The low excitation of the regions, as evidenced by the weakness of the [O III] λ5007 Å line (see left-hand panels of Figs 3, 4 and 5), precludes the detection and measurement of the auroral [O III] λ4363 Å necessary for the derivation of the electron temperature. It is therefore impossible to obtain a direct determination of the oxygen abundances. Empirical calibrations have to be used instead.

Different calibrators for strong emission lines have been proposed in the literature for different kinds of objects involving different chemical elements, among others, the oxygen abundance parameter $R_{23} \equiv O_{23}$ (Pagel et al. 1979), the nitrogen N2

Table 4. Equivalent widths of Balmer absorption lines for the observed CNSFR.

Galaxy	Region	Hδ (Å)	Corr. factor	Hγ (Å)	Corr. factor	Hβ (Å)	Corr. factor
NGC 2903	R1+R2	2.3	1.15	3.1	1.17	2.9	1.09
	R3	2.8	1.17	3.6	1.21	3.5	1.09
	R4	4.5	–	3.8	1.08	4.8	1.24
	R6	3.0	1.04	2.6	1.06	3.9	1.18
NGC 3351	R1	2.1	1.16	1.6	1.14	3.0	1.08
	R2	2.4	1.30	1.2	1.09	3.2	1.06
	R3	2.5	1.16	1.2	1.07	1.2	1.03
	R4	2.1	1.04	1.2	1.08	2.5	1.07
	R5	3.7	–	2.5	–	3.7	1.27
	R6	2.4	1.32	2.0	1.04	3.5	1.13
	R7	2.4	1.26	2.1	1.17	3.4	1.09
NGC 3504	R3+R4	4.5	1.25	3.6	1.18	4.4	1.10

Table 5. Reddening corrected emission line intensities for the CNSFR in NGC 2903.

Region			R1+R2		R3		R4		R6	
λ (Å)	Line	f_λ	f_λ	I_λ	f_λ	I_λ	f_λ	I_λ	f_λ	I_λ
3727	[O II]	0.271	267 ± 27	428 ± 44	333 ± 33	430 ± 45	421 ± 42	841 ± 88	198 ± 20	310 ± 31
4102	Hδ	0.188	179 ± 11	248 ± 16	235 ± 16	280 ± 19	–	–	145 ± 9	197 ± 13
4340	Hγ	0.142	432 ± 13	552 ± 17	553 ± 18	632 ± 20	164 ± 17	235 ± 24	298 ± 10	377 ± 13
4686	He II	0.045	5 ± 2	6 ± 3	–	–	–	–	11 ± 4	12 ± 4
4861	Hβ	0.000	1000 ± 16	1000 ± 16	1000 ± 21	1000 ± 21	1000 ± 27	1000 ± 28	1000 ± 13	1000 ± 13
4959	[O III]	−0.024	43 ± 6	41 ± 5	78 ± 5	76 ± 5	132 ± 84	125 ± 79	41 ± 3	40 ± 3
5007	[O III]	−0.035	131 ± 5	123 ± 5	229 ± 13	222 ± 12	391 ± 25	357 ± 23	122 ± 9	115 ± 8
5199	[N I]	−0.078	56 ± 8	49 ± 7	65 ± 26	60 ± 24	139 ± 45	114 ± 37	60 ± 15	53 ± 13
5876	He I	−0.209	79 ± 14	55 ± 10	97 ± 26	80 ± 21	–	–	97 ± 17	69 ± 12
6300	[O I]	−0.276	39 ± 6	24 ± 3	54 ± 13	41 ± 10	56 ± 14	28 ± 7	40 ± 13	25 ± 8
6312	[S III]	−0.278	7 ± 1	4 ± 1	–	–	–	–	–	–
6548	[N II]	−0.311	675 ± 11	394 ± 12	536 ± 16	400 ± 17	866 ± 62	391 ± 31	529 ± 17	318 ± 12
6563	Hα	−0.313	4897 ± 45	2850 ± 26	3826 ± 43	2850 ± 32	6341 ± 50	2850 ± 22	4759 ± 38	2850 ± 23
6584	[N II]	−0.316	2082 ± 19	1206 ± 33	1679 ± 47	1247 ± 54	2666 ± 66	1189 ± 52	1707 ± 26	1017 ± 27
6678	He I	−0.329	8 ± 3	4 ± 2	–	–	–	–	–	–
6717	[S II]	−0.334	498 ± 14	280 ± 11	472 ± 28	345 ± 24	811 ± 34	346 ± 20	528 ± 15	306 ± 11
6731	[S II]	−0.336	432 ± 16	242 ± 11	391 ± 24	285 ± 20	699 ± 31	297 ± 18	450 ± 16	260 ± 11
8863	P11	−0.546	36 ± 8	14 ± 3	–	–	–	–	–	–
9016	P10	−0.557	46 ± 7	18 ± 3	–	–	–	–	53 ± 14	21 ± 6
9069	[S III]	−0.561	157 ± 10	60 ± 5	103 ± 9	61 ± 6	220 ± 33	53 ± 9	137 ± 11	55 ± 5
9230	P9	−0.572	61 ± 8	23 ± 3	–	–	–	–	87 ± 16	34 ± 6
9532	[S III]	−0.592	393 ± 16	141 ± 9	337 ± 16	193 ± 15	508 ± 53	112 ± 14	450 ± 29	171 ± 13
9547	P8	−0.593	128 ± 14	46 ± 5	128 ± 17	73 ± 11	305 ± 58	67 ± 14	192 ± 20	73 ± 8
c(Hβ)			0.75 ± 0.04		0.41 ± 0.05		1.11 ± 0.05		0.71 ± 0.03	
I(Hβ)[a]				13.7 ± 0.22		1.80 ± 0.04		7.76 ± 0.21		6.84 ± 0.09
EW(Hβ)(Å)				12.7 ± 0.2		8.2 ± 0.2		2.6 ± 0.1		9.6 ± 0.2

[a] In units of 10^{-14} erg s^{-1} cm^{-2}.

Table 6. Reddening corrected emission line intensities for the CNSFR in NGC 3351.

Region			R1		R2		R3		R4	
λ (Å)	Line	f_λ	f_λ	I_λ	f_λ	I_λ	f_λ	I_λ	f_λ	I_λ
3727	[O II]	0.271	282 ± 28	455 ± 46	172 ± 17	230 ± 23	226 ± 23	336 ± 34	188 ± 19	271 ± 28
4102	Hδ	0.188	164 ± 7	229 ± 9	270 ± 7	330 ± 9	255 ± 6	335 ± 8	218 ± 13	281 ± 16
4340	Hγ	0.142	372 ± 8	478 ± 10	388 ± 8	452 ± 9	434 ± 7	534 ± 9	386 ± 14	467 ± 17
4686	He II	0.045	–	–	–	–	–	–	–	–
4861	Hβ	0.000	1000 ± 10	1000 ± 10	1000 ± 10	1000 ± 10	1000 ± 9	1000 ± 9	1000 ± 18	1000 ± 18
4959	[O III]	−0.024	36 ± 2	34 ± 2	47 ± 4	46 ± 4	27 ± 2	26 ± 2	28 ± 3	27 ± 3
5007	[O III]	−0.035	106 ± 6	100 ± 6	140 ± 6	135 ± 6	84 ± 4	79 ± 4	83 ± 8	79 ± 8
5199	[N I]	−0.078	49 ± 13	42 ± 11	61 ± 16	56 ± 14	38 ± 8	34 ± 7	61 ± 17	55 ± 15
5876	He I	−0.209	65 ± 12	45 ± 8	63 ± 27	51 ± 21	69 ± 10	51 ± 7	55 ± 10	41 ± 7
6300	[O I]	−0.276	24 ± 6	15 ± 4	31 ± 10	23 ± 7	19 ± 4	13 ± 3	19 ± 5	13 ± 3
6312	[S III]	−0.278	–	–	–	–	–	–	–	–
6548	[N II]	−0.311	565 ± 17	326 ± 12	476 ± 16	341 ± 14	584 ± 13	372 ± 11	457 ± 24	301 ± 18
6563	Hα	−0.313	4952 ± 48	2850 ± 28	3981 ± 42	2850 ± 30	4494 ± 37	2850 ± 24	4342 ± 45	2850 ± 30
6584	[N II]	−0.316	1739 ± 30	996 ± 27	1489 ± 21	1063 ± 27	1719 ± 19	1086 ± 23	1406 ± 34	919 ± 35
6678	He I	−0.329	16 ± 4	9 ± 2	5 ± 2	3 ± 2	15 ± 4	9 ± 3	–	–
6717	[S II]	−0.334	385 ± 9	214 ± 7	353 ± 13	247 ± 11	347 ± 6	213 ± 5	366 ± 18	233 ± 14
6731	[S II]	−0.336	353 ± 9	195 ± 7	337 ± 12	235 ± 10	330 ± 8	203 ± 6	322 ± 15	205 ± 11
8863	P11	−0.546	36 ± 5	14 ± 2	–	–	–	–	–	–
9016	P10	−0.557	53 ± 5	20 ± 2	18 ± 1	10 ± 1	40 ± 7	18 ± 3	24 ± 4	12 ± 2
9069	[S III]	−0.561	264 ± 15	98 ± 7	118 ± 7	65 ± 5	233 ± 13	103 ± 6	139 ± 13	66 ± 7
9230	P9	−0.572	92 ± 6	33 ± 3	43 ± 5	23 ± 3	66 ± 7	29 ± 3	66 ± 51	31 ± 24
9532	[S III]	−0.592	697 ± 30	245 ± 14	301 ± 16	160 ± 11	581 ± 30	245 ± 15	346 ± 21	156 ± 13
9547	P8	−0.593	89 ± 5	31 ± 2	247 ± 2	131 ± 5	103 ± 1	43 ± 1	92 ± 7	42 ± 4
c(Hβ)			0.77 ± 0.03		0.46 ± 0.03		0.63 ± 0.02		0.58 ± 0.04	
I(Hβ)[a]				9.63 ± 0.10		8.87 ± 0.09		11.4 ± 0.11		3.41 ± 0.06
EW(Hβ)(Å)				14.6 ± 0.2		9.5 ± 0.1		18.1 ± 0.3		12.3 ± 0.3

Table 6 – *continued*

Region			R5		R6		R7	
λ (Å)	Line	f_λ	f_λ	I_λ	f_λ	I_λ	f_λ	I_λ
3727	[O II]	0.271	348 ± 35	521 ± 61	350:	495:	196:	284:
4102	Hδ	0.188	–	–	85 ± 6	109 ± 7	193 ± 9	249 ± 11
4340	Hγ	0.142	–	–	262 ± 11	315 ± 13	400 ± 10	486 ± 12
4686	He II	0.045	–	–	–	–	12 ± 4	12 ± 5
4861	Hβ	0.000	1000 ± 37	1000 ± 37	1000 ± 20	1000 ± 20	1000 ± 13	1000 ± 13
4959	[O III]	−0.024	138 ± 13	134 ± 12	32:	31:	34 ± 2	33 ± 2
5007	[O III]	−0.035	409 ± 37	388 ± 35	96:	91:	100 ± 7	96 ± 7
5199	[N I]	−0.078	78 ± 33	70 ± 29	61 ± 19	55 ± 17	61 ± 13	55 ± 12
5876	He I	−0.209	–	–	–	–	36 ± 8	27 ± 6
6300	[O I]	−0.276	47 ± 14	31 ± 10	–	–	14 ± 5	9 ± 4
6312	[S III]	−0.278	–	–	–	–	–	–
6548	[N II]	−0.311	622 ± 43	391 ± 39	420 ± 28	282 ± 20	412 ± 17	269 ± 13
6563	Hα	−0.313	4543 ± 52	2850 ± 95	4259 ± 44	2850 ± 30	4382 ± 34	2850 ± 22
6584	[N II]	−0.316	1928 ± 109	1204 ± 109	1272 ± 55	848 ± 45	1289 ± 29	835 ± 26
6678	He I	−0.329	–	–	–	–	7 ± 3	4 ± 2
6717	[S II]	−0.334	548 ± 37	333 ± 34	275 ± 18	180 ± 13	345 ± 12	218 ± 9
6731	[S II]	−0.336	487 ± 33	295 ± 30	248 ± 17	161 ± 12	325 ± 11	205 ± 8
8863	P11	−0.546	–	–	–	–	–	–
9016	P10	−0.557	–	–	–	–	22 ± 3	10 ± 1
9069	[S III]	−0.561	191 ± 20	83 ± 13	89 ± 13	43 ± 7	112 ± 13	52 ± 6
9230	P9	−0.572	88 ± 29	38 ± 13	36 ± 11	17 ± 5	66 ± 7	30 ± 4
9532	[S III]	−0.592	415 ± 39	172 ± 28	202 ± 12	95 ± 8	307 ± 29	136 ± 14
9547	P8	−0.593	–	–	74 ± 11	35 ± 6	87 ± 1	39 ± 2
c(Hβ)			0.65 ± 0.10		0.56 ± 0.043		0.60 ± 0.03	
I(Hβ)[a]				2.04 ± 0.07		3.26 ± 0.07		8.05 ± 0.10
EW(Hβ)(Å)				3.1 ± 0.1		4.9 ± 0.1		9.0 ± 0.2

[a]In units of 10^{-14} erg s^{-1} cm^{-2}.

parameter (Denicoló, Terlevich & Terlevich 2002) and the sulphur abundance parameter S_{23} (Díaz & Pérez-Montero 2000). Furthermore, calibrators involving a combination of emission lines of two elements have been proposed, such as [O III]/[N II] (Alloin et al. 1979), [Ar III]λ7135 Å/[O III] λ5007 Å and [S III]λ9069 Å/[O III] λ5007 Å (Stasińska 2006). Our CNSFR show very weak lines of [O III] which are measured with large errors. This is taken as evidence for high metallicity in these regions. This, in turn, may imply values of N/O larger than solar, due to the chemical evolution of the regions themselves and the increasing production of secondary nitrogen. Hence, we have considered the use of the N2 parameter unreliable for this kind of objects. On the other hand, the [S III] lines are seen to be strong as compared to the [O III] lines (see right-hand panels of Figs 3, 4 and 5). Recently, the combination of both the oxygen abundance, O_{23}, and sulphur abundance, S_{23}, parameters has been claimed to be a good metallicity indicator for high metallicity H II regions (Díaz & Pérez-Montero 2000; Pérez-Montero & Díaz 2005). From now onwards we will call this parameter SO_{23}, and is defined as

$$\mathrm{SO_{23}} = \frac{\mathrm{S_{23}}}{\mathrm{O_{23}}} = \frac{I([\mathrm{S\,II}]\lambda\lambda 6716, 6731) + I([\mathrm{S\,III}]\lambda\lambda 9069, 9532)}{I([\mathrm{O\,II}]\lambda\lambda 3727, 3729) + I([\mathrm{O\,III}]\lambda\lambda 4959, 5007)}.$$

This parameter is similar to the S_3 O_3 proposed by Stasińska (2006) but is, at first order, independent of geometrical (ionization parameter) effects. The amount of available data on sulphur emission lines is increasingly growing, especially in the high metallicity regime. This makes possible for the first time to calibrate the electron temperature of [S III] in terms of the SO_{23} parameter. To perform this calibration we have compiled all the data so far at hand with sulphur emission-line data both for the auroral and nebular lines at λ6312 Å and λλ9069, 9532 Å respectively. The sample comprises data on galactic (García-Rojas 2006) and extragalactic (Díaz et al. 1987; Vílchez et al. 1988; Pastoriza et al. 1993; Gonzalez-Delgado et al. 1994; González-Delgado et al. 1995; Garnett et al. 1997; Díaz et al. 2000; Castellanos, Díaz & Terlevich 2002; Kennicutt, Bresolin & Garnett 2003; Bresolin, Garnett & Kennicutt 2004; Bresolin et al. 2005) H II regions and H II galaxies (Skillman & Kennicutt 1993; Skillman et al. 1994; Pérez-Montero & Díaz 2003; Hägele et al. 2006; Hägele et al. 2007b). The data on extragalactic H II regions has been further split into low and high metallicity H II regions according to the criterion of Díaz & Pérez-Montero (2000), i.e. $\log \mathrm{O_{23}} \leqslant 0.47$ and $-0.5 \leqslant \log \mathrm{S_{23}} \leqslant 0.28$ implies oversolar abundances. For all the regions the [S III] electron temperature has been derived from the ratio between the auroral and the nebular sulphur lines, using a five-level atom program (Shaw & Dufour 1995) and the collisional strengths from Tayal & Gupta (1999), through the task TEMDEN as implemented in the IRAF package. The calibration is shown in Fig. 9 together with the quadratic fit to the high metallicity H II region data:

$$t_\mathrm{e}([\mathrm{S\,III}]) = 0.596 - 0.283 \log \mathrm{SO_{23}} + 0.199(\log \mathrm{SO_{23}})^2.$$

Fig. 10 shows the comparison between the electron temperatures and ionic sulphur abundances derived from measurements of the auroral sulphur line λ6312 Å and our derived calibration. The S^+/H^+ and S^{2+}/H^+ ionic ratios have been derived from

$$12 + \log \frac{\mathrm{S^+}}{\mathrm{H^+}} = \log\left(\frac{I(6717) + I(6731)}{I(\mathrm{H}\beta)}\right) + 5.423 + \tfrac{0.929}{t} - 0.28 \log t,$$

Table 7. Reddening corrected emission line intensities for the CNSFR in NGC 3504.

Region			R3+R4	
λ (Å)	Line	f_λ	f_λ	I_λ
3727	[O II]	0.271	953 ± 95	1395 ± 141
4102	Hδ	0.188	250 ± 5	326 ± 7
4340	Hγ	0.142	460 ± 6	561 ± 8
4686	He II	0.045	–	–
4861	Hβ	0.000	1000 ± 8	1000 ± 8
4959	[O III]	−0.024	63 ± 4	61 ± 4
5007	[O III]	−0.035	192 ± 8	183 ± 7
5199	[N I]	−0.078	69 ± 15	62 ± 13
5876	He I	−0.209	87 ± 11	65 ± 8
6300	[O I]	−0.276	80 ± 7	54 ± 5
6312	[S III]	−0.278	–	–
6548	[N II]	−0.311	818 ± 17	529 ± 13
6563	Hα	−0.313	4423 ± 29	2850 ± 19
6584	[N II]	−0.316	2466 ± 29	1583 ± 30
6678	He I	−0.329	17 ± 4	11 ± 3
6717	[S II]	−0.334	652 ± 13	408 ± 10
6731	[S II]	−0.336	599 ± 12	374 ± 9
8863	P11	−0.546	–	–
9016	P10	−0.557	34 ± 7	15 ± 3
9069	[S III]	−0.561	327 ± 13	149 ± 7
9230	P9	−0.572	95 ± 8	43 ± 4
9532	[S III]	−0.592	802 ± 25	350 ± 15
9547	P8	−0.593	–	–
c(Hβ)			0.61 ± 0.02	
I(Hβ)[a]				20.8 ± 0.17
EW(Hβ)(Å)				15.2 ± 0.2

[a] In units of 10^{-14} erg s^{-1} cm^{-2}.

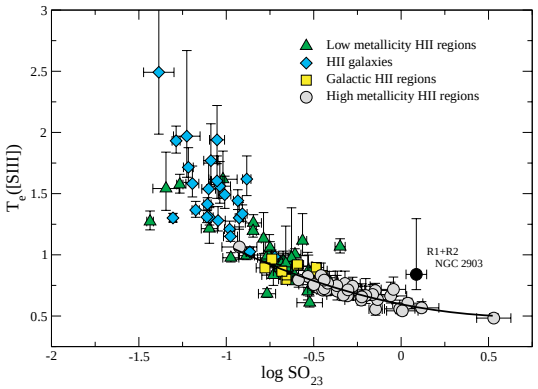

Figure 9. Empirical calibration of the [S III] electron temperature as a function of the abundance parameter SO_{23} defined in the text. The solid line represents a quadratic fit to the high metallicity H II region data. References for the data are given in the text.

$$12 + \log \frac{S^{2+}}{H^+} = \log\left(\frac{I(9069) + I(9532)}{I(H\beta)}\right) + 5.8 + \frac{0.771}{t} - 0.22 \log t.$$

These expressions have been derived by performing appropriate fittings to the IONIC task results following the functional form given in Pagel et al. (1992). The assumption has been made that T_e[S III] $\simeq T_e$([S II]) in the observed regions. This assumption seems to be justified in view of the results presented by Bresolin et al. (2005).

We have used the calibration above to derive t_e([S III]) for our observed CNSFR. In all cases the values of $\log O_{23}$ are inside the range used in performing the calibration, thus requiring no extrapolation of the fit. These temperatures, in turn, have been used to derive the S^+/H^+ and S^{2+}/H^+ ionic ratios. The derived T_e and ionic abundances for sulphur are given in Table 8, together with measured values of the electron density. Temperature and abundance errors are formal errors calculated from the measured line intensity errors applying error propagation formulae, without assigning any error to the temperature calibration itself.

Once the sulphur ionic abundances have been derived, we have estimated the corresponding oxygen abundances. In order to do that, we have assumed that sulphur and oxygen electron temperatures follow the relation given by Garnett (1992) and confirmed by more recent data (Hägele et al. 2006), and hence we have derived t_e([O III]) according to the expression

$$t_e([O\,III]) = 1.205\, t_e([S\,III]) - 0.205.$$

We have also assumed that t_e([O II]) $\simeq t_e$([S III]). The values of T_e([O III]) and the ionic abundances for oxygen are given in Table 9. The same comments regarding errors mentioned above apply. Finally, we have derived the N^+/O^+ ratio assuming that t_e([O II]) $\simeq$ t_e([N II]) $\simeq t_e$([S III]). These values are also listed in Table 9.

For one of the observed regions, R1+R2 in NGC 2903, the [S III] λ6312 Å has been detected and measured. Although the line intensity ratios for this region presented in Table 5 have been measured on the combined spectrum of slit positions 1 and 2, the placement of the continuum for the [S III] 6312 line was very uncertain. Therefore, we have performed the temperature measurement on the spectrum extracted from slit position 1, which shows the best-defined continuum. On this spectrum we have measured the intensity of the [S III] λ6312 Å line with respect to Hα, and those of [S III] λλ9069, 9532 Å with respect to P9 λ9329, in order to minimize reddening corrections. The region of this spectrum around the [S III] λ6312 Å line is shown in Fig. 11 where the horizontal lines show the different placements of the continuum used to measure the line and calculate the corresponding errors. The obtained [S III] nebular to auroral line ratio is 79.4 ± 49.1 which gives a $T_e([S\,III]) = 8400^{+4650}_{-1250}$ K, slightly higher than predicted by the proposed fit. This region is represented as a solid black circle in Fig. 9.

6 DISCUSSION

6.1 Characteristics of the observed CNSFR

Planesas et al. (1997) provide Hα fluxes (from images) for all our observed regions. These values are larger than those measured inside our slit by factors between 1.0 and 2.7, depending on the size of the region, something to be expected given the long-slit nature of our observations. We have calculated the Hα luminosities for our regions from our observed values, correcting for extinction according to the values found from the spectroscopic analysis. The resulting values are listed in Table 10. These values are larger than the typical ones found for disc H II regions and overlap with those measured in H II galaxies. The region with the largest Hα luminosity is R3+R4 in NGC 3504, for which a value of 2.02×10^{40} erg s^{-1} is measured.

We have derived the number of hydrogen ionizing photons from the extinction corrected Hα flux as

$$\log Q(H^0) = 0.802 \times 10^{49} \left(\frac{F(H\alpha)}{10^{-14}}\right)\left(\frac{D}{10}\right) s^{-1},$$

where F(Hα) is in erg cm^{-2} s^{-1} and the distance, D, is in Mpc.

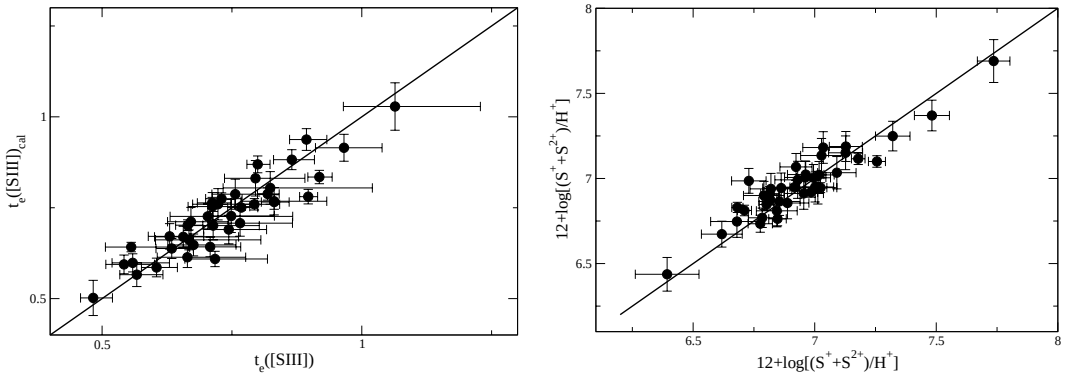

Figure 10. Comparison between the electron temperatures (left) and ionic abundances for sulphur (right) for the high metallicity H II region sample, as derived from measurements of the auroral sulphur line λ6312 Å (abscissa) and from our derived calibration (ordinate). The solid line represents the one-to-one relation.

Table 8. Derived electron densities, electron temperatures and ionic abundances from sulphur lines in our observed CNSFR.

Galaxy	Region	n_e (cm^{-3})	T_e([S III]) (K)	$12 + \log(S^+/H^+)$	$12 + \log(S^{2+}/H^+)$	$12 + \log[(S^+ + S^{2+})/H^+]$
NGC 2903	R1+R2	280 ± 90	5731 ± 188	6.83 ± 0.04	6.50 ± 0.05	7.01 ± 0.05
	R3	230 ± 135	5737 ± 210	6.91 ± 0.06	6.60 ± 0.06	7.09 ± 0.06
	R4	270 ± 120	6660 ± 331	6.68 ± 0.06	6.21 ± 0.08	6.81 ± 0.06
	R6	250 ± 80	5413 ± 221	6.97 ± 0.05	6.64 ± 0.06	7.14 ± 0.05
NGC 3351	R1	360 ± 80	5683 ± 188	6.74 ± 0.04	6.75 ± 0.05	7.05 ± 0.04
	R2	440 ± 110	5405 ± 210	6.90 ± 0.05	6.65 ± 0.06	7.09 ± 0.05
	R3	430 ± 70	5399 ± 210	6.84 ± 0.04	6.83 ± 0.05	7.14 ± 0.05
	R4	310 ± 120	5390 ± 271	6.87 ± 0.06	6.64 ± 0.07	7.07 ± 0.07
	R5	360 ± 230	6177 ± 286	6.78 ± 0.07	6.49 ± 0.09	6.97 ± 0.08
	R6	360 ± 170	6297 ± 295	6.49 ± 0.06	6.20 ± 0.07	6.67 ± 0.07
	R7	410 ± 100	5537 ± 220	6.80 ± 0.05	6.52 ± 0.07	6.99 ± 0.06
NGC 3504	R3+R4	370 ± 60	6288 ± 170	6.86 ± 0.03	6.77 ± 0.03	7.12 ± 0.03

Table 9. Derived T_e and ionic abundances for oxygen and nitrogen in our observed CNSFR.

Galaxy	Region	T_e([O III]) (K)	$12 + \log(O^+/H^+)$	$12 + \log(O^{2+}/H^+)$	$12 + \log[(O^+ + O^{2+})/H^+]$	$\log(N^+/O^+)$
NGC 2903	R1+R2	4855 ± 226	8.55 ± 0.08	8.11 ± 0.08	8.69 ± 0.08	−0.37 ± 0.07
	R3	4863 ± 253	8.55 ± 0.09	8.37 ± 0.09	8.77 ± 0.09	−0.36 ± 0.08
	R4	5975 ± 399	8.42 ± 0.10	8.04 ± 0.14	8.57 ± 0.11	−0.50 ± 0.08
	R6	4473 ± 267	8.59 ± 0.10	8.33 ± 0.10	8.79 ± 0.10	−0.38 ± 0.07
NGC 3351	R1	4798 ± 227	8.60 ± 0.08	8.06 ± 0.08	8.72 ± 0.08	−0.49 ± 0.07
	R2	4463 ± 253	8.47 ± 0.09	8.41 ± 0.10	8.74 ± 0.09	−0.23 ± 0.07
	R3	4456 ± 253	8.64 ± 0.09	8.17 ± 0.10	8.77 ± 0.09	−0.38 ± 0.07
	R4	4445 ± 327	8.55 ± 0.11	8.19 ± 0.13	8.71 ± 0.12	−0.37 ± 0.08
	R5	5393 ± 344	8.42 ± 0.10	8.34 ± 0.10	8.68 ± 0.10	−0.37 ± 0.10
	R6	5538 ± 356	8.34 ± 0.10	7.62 ± 0.17	8.42 ± 0.11	−0.47 ± 0.08
	R7	4622 ± 266	8.48 ± 0.09	8.15 ± 0.10	8.65 ± 0.10	−0.40 ± 0.07
NGC 3504	R3+R4	5527 ± 205	8.79 ± 0.07	7.94 ± 0.06	8.85 ± 0.07	−0.65 ± 0.06

The ionization parameter, u, can be estimated from the [S II]/[S III] ratio (Díaz et al. 1991) as

$$\log u = -1.68 \log([\mathrm{S\,II}]/[\mathrm{S\,III}]) - 2.99,$$

and ranges between −3.12 and −3.98 for our observed CNSFR, in the low side of what is found in disc H II regions, even in the cases of high metallicity (see Díaz et al. 1991).

From the calculated values of the number of Lyman α photons, $Q(H^0)$, ionization parameter and electron density, it is possible to derive the size of the emitting regions as well as the filling factor (see Castellanos et al. 2002). The derived sizes are between 1.5 arcsec for region R3 in NGC 3351 and 5.7 arcsec for region R4 in NGC 2903; these values correspond to linear dimensions between 74 and 234 pc. The derived filling factors are low: between 6×10^{-4} and 1×10^{-3}, lower than commonly found in giant H II regions (∼0.01). Sizes in arcsec, filling factors and the corresponding masses of ionized hydrogen, M(H II), are given in Table 10.

We have also derived the mass of ionizing stars, M^*, from the calculated number of hydrogen ionizing photons with the use of evolutionary models of ionizing clusters (García Vargas & Díaz 1994; Stasińska & Leitherer 1996) assuming that the regions are ionization bound and that no photons are absorbed by dust. A Salpeter initial

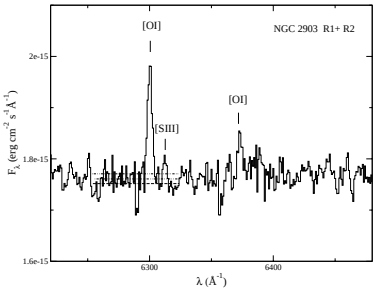

Figure 11. Spectrum of region R1+R2 in NGC 2903 around [S III] λ6312 Å. The way in which the [S III] line has been measured is shown. The different continuum placements used for the computation of the errors are shown by horizontal lines.

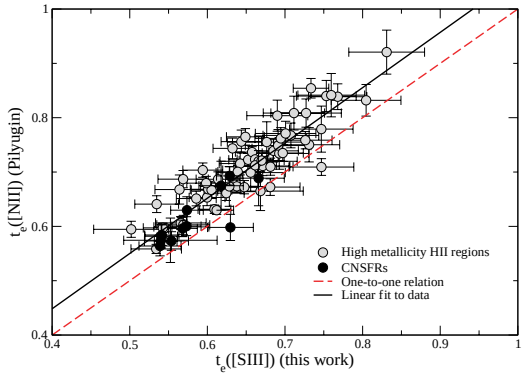

Figure 12. t_e([N II]) derived from Pilyugin's method against the t_e([S III]) derived from the calibration presented in this work. The dashed line shows the one-to-one correspondence.

mass function (IMF) with upper and lower mass limits of 100 and 0.8 $M_\odot$, respectively, has been assumed. According to these models, a relation exists between the degree of evolution of the cluster, as represented by its Hβ emission line equivalent width and the number of hydrogen ionizing photons per unit solar mass (Díaz 1998; Díaz et al. 2000). The ionizing cluster masses thus derived are given in Table 10 and range between 1.1×10^5 and 4.7×10^6 $M_\odot$. The measured Hβ equivalent widths, however, are very low and could be reflecting the contribution by underlying non-ionizing populations. An alternative way to take into account the cluster evolution in the derivation of the mass is to make use of the existing relation between the ionization parameter and the Hβ equivalent width for ionized regions (Hoyos & Díaz 2006). In that case, the derived masses are lower by factors between 1.5 and 15. At any rate, given the assumptions of no dust absorption or photon leakage, these masses represent lower limits.

6.2 Metallicity estimates

The abundances we derive using our T_e([S III]) calibration are comparable to those found by Bresolin et al. (2004) for their sample of high metallicity H II regions. Most of our CNSFR show total oxygen abundances, taken to be $O/H = O^+/H^+ + O^{2+}/H^+$, consistent with solar values within the errors. The region with the highest oxygen abundance is R3+R4 in NGC 3504: 12+log(O/H) = 8.85, about 1.5 solar if the solar oxygen abundance is set at the value derived by Asplund, Grevesse & Sauval (2005), $12 + \log(O/H)_\odot = 8.66 \pm 0.05$. Region R6 in NGC 3351 has the lowest oxygen abundance of the sample, about 0.6 times solar. In all the observed CNSFR the O/H abundance is dominated by the O^+/H^+ contribution with $0.18 \leqslant \log(O^+/O^{2+}) \leqslant 0.85$. This is also the case for high metallicity disc H II regions where these values are even higher. For our observed regions, also the S^+/S^{2+} ratios are larger than one, which is at odds with the high metallicity disc H II regions for which, in general, the sulphur abundances are dominated by S^{2+}/H^+.

The fact that both O/H and S/H seem to be dominated by the lower ionization species, can raise concern about our method of abundance derivation, based on the calibration of the T_e([S III]). In a recent article Pilyugin (2007) addresses this particular problem. He proposes a calibration of the ratio of the [N II] nebular-to-auroral line intensities in terms of those of the nebular oxygen lines. Then the [N II] electron temperature, thought to properly characterize the low ionization zone of the nebula, can be obtained. We have applied Pilyugin (2007) to our observed CNSFR as well as the high metallicity H II sample. Fig. 12 shows the derived t_e([N II]) following Pilyugin's method against the t_e([S III]) derived from our calibration. The (red) dashed line shows the one-to-one relation while the (black) solid line shows the actual fit to all the data. It can be seen that, in what regards CNSFR, both temperatures are very similar, with the [N II] temperature being, in average, 500 K higher than that of [S III]. This difference is of the same size of the average errors in the measured temperatures entering the calibrations, therefore, we can assume that our derived t_e([S III]) characterizes the low ionization zone at least as well as the t_e([N II]) derived applying Pilyugin's method.

Table 10. General properties of the observed CNSFR.

Galaxy	Region	F(Hα) (erg cm^{-2} s^{-1})	L(Hα) (erg s^{-1})	Q(H^0) (photon s^{-1})	log u	Diameter (arcsec)	ϵ	M^* ($M_\odot$)	M(H II) ($M_\odot$)
NGC 2903	R1+R2	3.06E-13	2.71E+39	1.98E+51	−3.69	4.66	5.93E-04	7.39E+05	1.44E+04
	R3	3.16E-14	2.80E+38	2.05E+50	−3.65	1.59	2.29E-03	1.11E+05	1.81E+03
	R4	2.23E-13	1.98E+39	1.45E+51	−3.98	5.70	2.54E-04	2.11E+06	1.09E+04
	R6	1.48E-13	1.31E+39	9.60E+50	−3.66	3.33	9.89E-04	4.55E+05	7.79E+03
NGC 3351	R1	2.19E-13	2.65E+39	1.94E+51	−3.12	1.81	3.76E-03	6.40E+05	1.09E+04
	R2	1.61E-13	1.95E+39	1.42E+51	−3.55	2.29	9.08E-04	6.80E+05	6.56E+03
	R3	2.35E-13	2.84E+39	2.08E+51	−3.12	1.72	3.31E-03	5.70E+05	9.80E+03
	R4	6.84E-14	8.29E+38	6.06E+50	−3.49	1.66	2.04E-03	2.32E+05	3.96E+03
	R5	4.25E-14	5.15E+38	3.76E+50	−3.65	1.47	1.37E-03	4.71E+05	2.12E+03
	R6	6.43E-14	7.79E+38	5.70E+50	−3.65	1.81	1.11E-03	4.81E+05	3.21E+03
	R7	1.60E-13	1.94E+39	1.42E+51	−3.58	2.47	8.31E-04	7.11E+05	7.03E+03
NGC 3504	R3+R4	4.20E-13	2.02E+40	1.47E+52	−3.32	3.11	6.76E-04	4.70E+06	8.07E+04

Concerning relative abundances, with our analysis it is possible to derive the relative N/O value, assumed to be equal to the N^+/O^+ ratio. These values are in all cases larger than the solar one ($\log(N/O)_\odot = -0.88$; Asplund et al. 2005) by factors between 1.7 (R3+R4 in NGC 3504) and 4.5 (R2 in NGC 3351) which are amongst the highest observed N/O ratios (see e.g. Mollá et al. 2006). Regarding S, if – given the low excitation of the observed regions – the fraction of S^{3+} is assumed to be negligible, the S/O ratio can be obtained as

$$\frac{S}{O} = \frac{S^+ + S^{2+}}{O^+ + O^{2+}}.$$

The values of log(S/O) span a very narrow range between -1.76 and -1.63, that is between 0.6 and 0.8 of the solar value $\log(S/O)_\odot = -1.52$;(Asplund et al. 2005).

6.3 Comparison with high metallicity H II regions

The observed CNSFR being of high metallicity show however marked differences with respect to high metallicity disc H II regions. Even though their derived oxygen and sulphur abundances are similar, they show values of the O_{23} and the N2 parameters whose distributions are shifted to lower and higher values, respectively, with respect to the high metallicity disc sample (Fig. 13). Hence, if pure empirical methods were used to estimate the oxygen abundances for these regions, higher values would in principle be obtained. This would seem to be in agreement with the fact that CNSFR, when compared to the disc high metallicity regions, show the highest [N II]/[O II] ratios. Fig. 14 shows indeed a bi-modal distribution of the [N II]/[O II] ratio in disc and circumnuclear H II regions.

A good correlation has been found to exist between the [N II]/[O II] ratio and the N^+/O^+ ionic abundance ratio, which in turn can be assumed to trace the N/O ratio (Pérez-Montero & Díaz 2005). This relation is shown in Fig. 15 for the observed CNSFR (black circles) and the high metallicity H II region sample (grey circles). The CNSFR sample has been enlarged with two circumnuclear regions of NGC 1097 observed by Phillips et al. (1984) and other three observed in NGC 5953 by Gonzalez Delgado & Perez (1996), all of them of high metallicity. Also shown are data of some CNSFR in two peculiar galaxies: NGC 3310 (Pastoriza et al. 1993) and NGC 7714 (González-Delgado et al. 1995) of reported lower metallicity. In all the cases, ionic and total abundances have been derived following the same methods as in the CNSFR in the present study and described in Section 5. In the case of the latter regions, abundances derived in this way are larger than derived from direct determinations of $t_e([O\,III])$ since our estimated values for this temperature are systematically lower by about 1200 K. This could be due to the fact that our semi-empirical calibration has been actually derived for high metallicity regions. However, the values of $\log(SO_{23})$ for these regions are between -0.44 and -0.85 and therefore within the validity range of the calibration and we have preferred to use the same method for consistency reasons.

We can see that a very tight correlation exists which allows to estimate the N/O ratio from the measured [N II] and [O II] emission line intensities. In this relation, high metallicity regions and

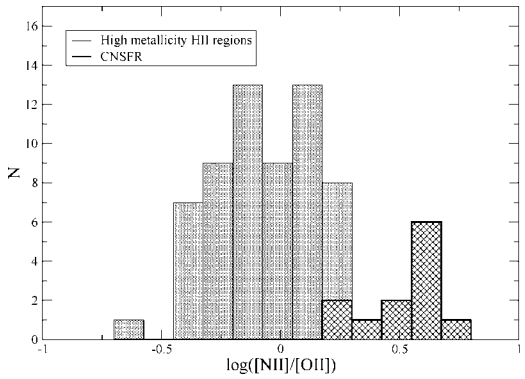

Figure 14. Distribution of the [N II]/[O II] ratio for the observed CNSFR (criss-crossed) and the sample of high metallicity disc H II regions (hatched).

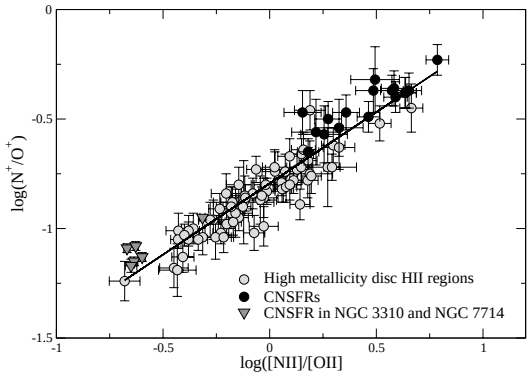

Figure 15. The relation between the [N II]/[O II] emission line intensity ratio and the N^+/O^+ ratio for CNSFR (black circles) and high metallicity H II regions (grey circles). Included also (downward triangles) are lower metallicity CNSFR in NGC 3310 (Pastoriza et al. 1993) and NGC 7714 (González-Delgado et al. 1995).

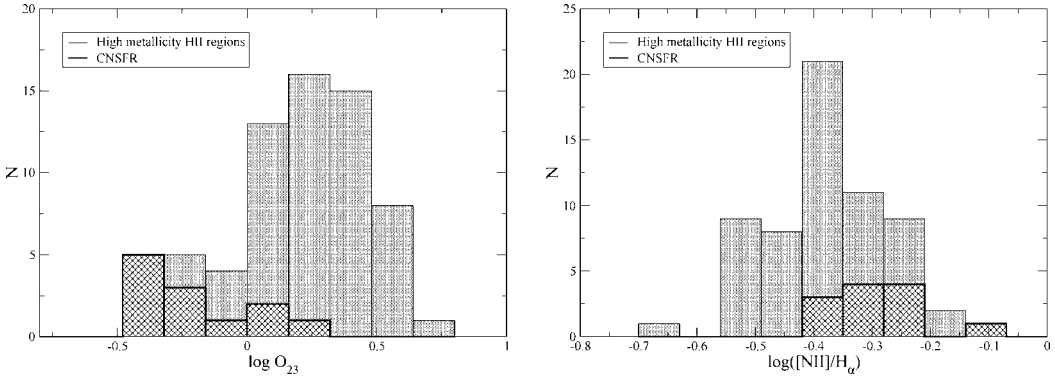

Figure 13. Distribution of the empirical abundance parameters O_{23} (left) and N2 (right) for the observed CNSFR and the sample of high metallicity disc H II regions.

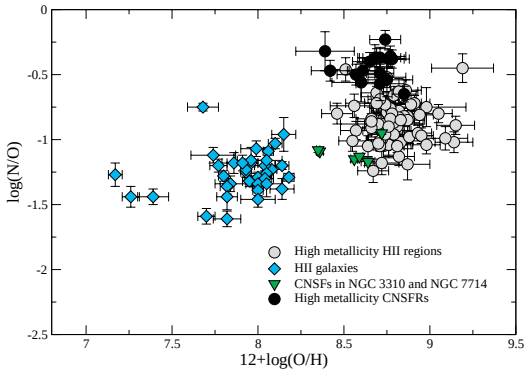

Figure 16. Relation between the N/O ratio and the O/H abundance for CNSFR (black circles and green upside down triangles for high and low metallicities, respectively), high metallicity H II regions (grey circles) and H II galaxies (cyan diamonds).

CNSFR seem to follow a sequence of increasing N/O ratio. A linear regression fit to the data yields the expression:

$$\log(\mathrm{N/O}) = (0.65 \pm 0.02)\log([\mathrm{N\,II}]/[\mathrm{O\,II}]) - (0.79 \pm 0.01).$$

This relation is shallower than that found in Pérez-Montero & Díaz (2005) for a sample that did not include high metallicity H II regions. The N/O ratio for our observed CNSFR is shown in Fig. 16 against their oxygen abundance together with similar data for the high metallicity H II region and H II galaxy samples. It can be seen that all the CNSFR show similar oxygen abundances, with the mean value being lower than that shown by high metallicity disc H II regions, but the observed CNSFR show larger N/O ratios and they do not seem to follow the trend of N/O versus O/H which marks the secondary behaviour of nitrogen.

The values of the oxygen abundance that we find for the CNSFR in NGC 3351 are equal within the errors, with a mean value $12 + \log(\mathrm{O/H}) = 8.70 \pm 0.10$, except for region R6 which shows an O/H abundance lower by a factor of about 2. It is worth noting that this is the region with the highest $\mathrm{O^+/O}$ ratio: 0.83 and a very low $\mathrm{O^{2+}/H^+}$ value: $12 + \log(\mathrm{O^{2+}/H^+}) = 7.62 \pm 0.17$. The average value for the rest of the regions is in agreement with the central abundance found by Pilyugin, Thuan & Vílchez (2006) by extrapolating the galaxy oxygen abundance gradient, $12 + \log(\mathrm{O/H}) = 8.74 \pm 0.02$. This value is somewhat lower than that previously estimated by Pilyugin, Vílchez & Contini (2004): 8.90 from the same data but following a different method of analysis. In that same work, the quoted central abundance for NGC 2903 is $12 + \log(\mathrm{O/H}) = 8.94$. Our results for regions R1+R2, R3 and R6 in this galaxy yield an average value of 8.75 ± 0.09 lower than theirs by 0.2 dex. Region R4 shows a lower oxygen abundance but still consistent within the errors with the average. Values of N/O ratios for the centres of NGC 3351 and NGC 2903 similar to those found here (-0.33 and -0.35, respectively) are quoted by Pilyugin et al. (2004).

Another difference between the high metallicity circumnuclear and disc regions is related to their average ionization parameter. The left-hand panel of Fig. 17 shows the distribution of the [S II]/[S III] ratio for the two samples. The [S II]/[S III] ratio has been shown to be a good ionization parameter indicator for moderate to high metallicities (Díaz et al. 1991) with very little dependence on metallicity or ionization temperature. It can be seen that all the CNSFR observed show large [S II]/[S III] ratios which imply extremely low ionization parameters. On the other hand, a different answer would be found if the [O II]/[O III] parameter, also commonly used as ionization parameter indicator, was used. In this case, CNSFR and high metallicity H II regions show a much more similar distribution, with CNSFR showing slightly lower values of [O II]/[O III] (Fig. 17, right-hand panel).

It should be noted the dependence of the [O II]/[O III] parameter on metallicity due to the presence of opacity edges of various abundant elements ($\mathrm{O^+}$, $\mathrm{Ne^+}$, $\mathrm{C^{2+}}$, $\mathrm{N^{2+}}$) in the stellar atmospheres that can combine to substantially modify the stellar flux of high abundance stars at energies higher than 35–30 eV and then produce a lower [O III] emission (Balick & Sneden 1976). However, if the CNSFR were ionized by stars of a higher metallicity than those in disc H II regions this effect would go in the direction of producing higher [O II]/[O III] ratios for the CNSFR, and ionization parameters derived from [O II]/[O III] ratios would be found to be lower than those derived from [S II]/[S III] ratios, contrary to what is actually observed.

The ionization structure can provide important information about the characteristics of the ionizing source. A diagram of the emission line ratios [O II]/[O III] versus [S II]/[S III], in particular, works as a diagnostics for the nature and temperature of the radiation field. This diagram was used in Díaz, Pagel & Wilson (1985) in order to investigate the possible contributions by shocks in CNSFR and LINERs and is the basis of the definition of the η' parameter (Vilchez & Pagel 1988). The η' parameter defined as

$$\eta' = \frac{[\mathrm{O\,II}]\lambda\lambda 3727, 3729/[\mathrm{O\,III}]\lambda\lambda 4959, 5007}{[\mathrm{S\,II}]\lambda\lambda 6716, 6731/[\mathrm{S\,III}]\lambda\lambda 9069, 9532}$$

is a measure of the 'softness' of the ionizing radiation and increases with decreasing ionizing temperature. The 'η' plot' is shown in

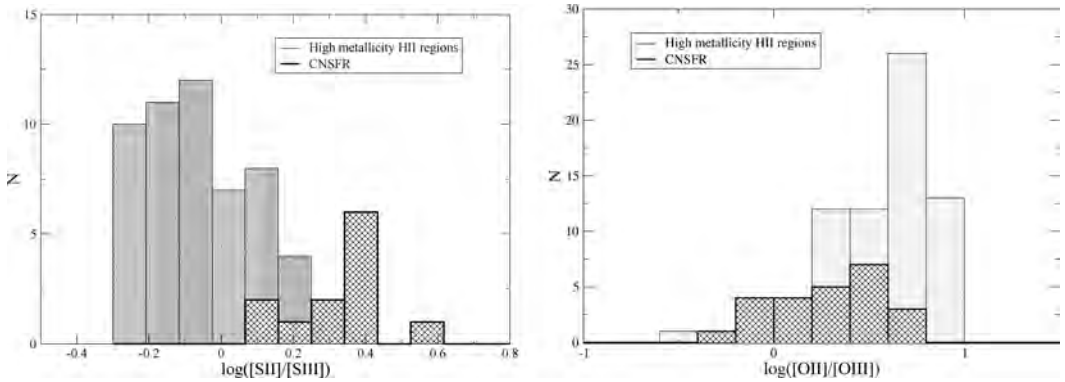

Figure 17. Distribution of the [S II]/[S III] (left) and [O II]/[O III] (right) ratios for the observed CNSFR (criss-crossed) and the sample of high metallicity disc H II regions (hatched).

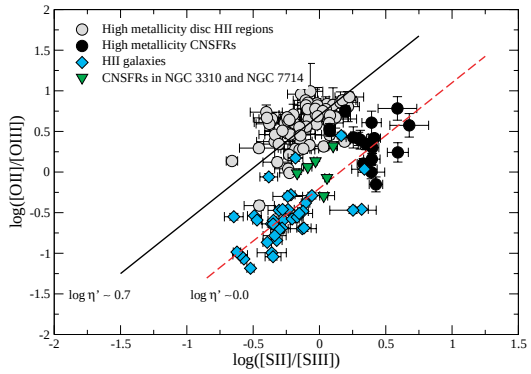

Figure 18. The η' plot: the [O II]/[O III] ratio versus [S II]/[S III] ratio for different ionized regions: high metallicity CNSFR (black circles), low metallicity CNSFR (green upside down triangles), high metallicity disc H II regions (grey circles) and H II galaxies (cyan diamonds).

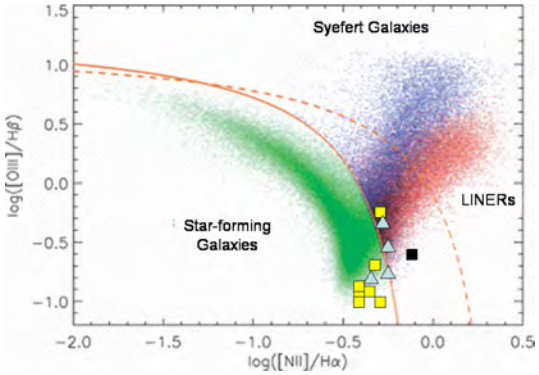

Figure 19. The [N II]/Hα versus [O III]/Hβ diagnostics for emission line objects in the SDSS (adapted from Groves et al. 2006). The location of our observed CNSFR is shown overplotted. Light (blue) triangles correspond to NGC 2903, light (yellow) squares correspond to NGC 3351 and the black square correspond to NGC 3504. Solid (Kewley et al. 2001) and dashed (Kauffmann et al. 2003) lines separate the star forming from the active nucleus galaxies regions.

Fig. 18. In this plot, diagonal lines of slope unity would show the locus of ionized regions with constant values of η'. The lines shown in the plot have slope 1.3 reflecting the second-order dependence of η' on ionization parameter (Díaz et al. 1991). In this graph CNSFR are seen to segregate from disc H II regions. The former cluster around the value of $\log \eta' = 0.0$ (T ion $\sim$ 40 000 K) while the latter cluster around $\log \eta' = 0.7$ (T ion $\sim$ 35 000 K). Also shown are the data corresponding to H II galaxies. Indeed, CNSFR seem to share more the locus of the H II galaxies than that of disc H II regions.

Given the problems involved in the measurement of the [O II] emission lines mentioned in Section 4.2 it is interesting to see the effects that a possible underestimate of the intensity of this line would have on our analysis. The underestimate of the [O II] line leads to an overestimate of the SO_{23} parameter and hence to an underestimate of the [S III] electron temperature. This lower temperature in turn leads to higher O/H abundances. Therefore, larger values of the intensity of the [O II] line would lead to lower O/H abundances, however, not by a large amount. Increasing the [O II] intensity by a factor of 2 would decrease the SO_{23} parameter by a factor between 1.5 and 1.8 depending on the region, which would lead to increased [S III] electron temperatures by between 500 and 1000 K. The corresponding O^+/H^+ would be only slightly smaller, by about 0.10 dex, as would also be the total O/H abundances which is dominated by O^+/H^+. The O^{2+}/H^+ ionic ratio however would be lower by between 0.3 and 0.4 dex, which would produce an ionization structure more similar to what is found in disc H II regions. The sulphur ionic and total abundances would be decreased by about 0.17 dex. Finally, the N^+/O^+ ratios would be decreased by about 0.17 dex, while the S/O ratios would remain almost unchanged. In the 'η' plot' (Fig. 18) the data points corresponding to our observed CNSFR would move upwards by 0.30 dex. However, we do not find any compelling reason why the [O II] intensities should be larger than measured by such a big amount (see Section 4.2 and Fig. 8).

One possible concern about these CNSFR is that, given their proximity to the galactic nuclei, they could be affected by hard radiation coming from a low luminosity active galactic nucleus (AGN). NGC 3551 shows a faint ultraviolet core. However, the *International Ultraviolet Explorer* (*IUE*) spectrum that covers the whole central star-forming ring shows broad absorption lines of Si IV λ1400 Å and C IV λ1549 Å typical of young stars of high metallicity (Colina et al. 1997). They are consistent with a total mass of 3×10^5 $M_\odot$ of recently formed stars (4–5 Myr). This is of the order of our derived values for single CNSFR in this galaxy. Therefore, no signs of activity are found for this nucleus nor are they reported for the other two galaxy nuclei. On the other hand, the He II λ4686 Å line is measured in regions R1+R2 and R6 of NGC 2903 and in region R7 in NGC 3351. In the first region, there is some evidence for the presence of Wolf–Rayet (WR) stars (Castellanos et al. 2002). For the other two, that presence is difficult to assess due to the difficulty in placing the continuum for which a detailed modelling of the stellar population is needed.

Alternatively, the spectra of these regions harbouring massive clusters of young stars might be affected by the presence of shocked gas. Diagnostic diagrams of the kind presented by Baldwin, Phillips & Terlevich (1981) can be used to investigate the possible contribution by either a hidden AGN or by the presence of shocks to the emission line spectra of the observed CNSFR. Fig. 19 shows one of these diagnostic diagrams, log ([N II]/Hα) versus log ([O III])/Hβ, for our CNSFR: light squares for NGC 3351, triangles for NGC 2903 and dark square for NGC 3504. The figure has been adapted from Groves, Heckman & Kauffmann (2006) and shows the location of emission-line galaxies in the Sloan Digital Sky Survey (SDSS). Dashed and solid lines correspond to the boundary between AGN and H II galaxies defined by Kewley et al. (2001) and Kauffmann et al. (2003), respectively. Some of our observed CNSFR are found close to the transition zone between H II region and LINER spectra but only R3+R4 in NGC 3504 may show a hint of a slight contamination by shocks. This region, the most luminous in our sample and also the one with the highest abundance, should be studied in more detail.

A final remark concerns the gas kinematics in CNSFR. In a recent work Hägele et al. (2007a) have studied the kinematics of gas and stars in the CNSFR of NGC 3351 finding two different components for the ionized gas in Hβ and [O III] emission: a 'broad component' with a velocity dispersion similar to that measured for the stars, and a 'narrow component' with a dispersion lower than the stellar one by about 30 km s^{-1}. Obviously the abundance analysis and the location of these regions on diagnostic diagrams would be affected if more than one velocity component in the ionized gas corresponding to kinematically distinct systems are present.

7 SUMMARY AND CONCLUSIONS

We have obtained spectrophotometric observations in the optical (λλ3650–7000 Å) and far-red (λλ8850–9650 Å) wavelength ranges of 12 circumnuclear H II regions in the early-type spiral galaxies: NGC 2903, 3351 and 3504. These regions were expected to be amongst the highest metallicity regions as corresponds to their position near the galactic centre. At the same time, this position implies a substantial contribution by the bulge stellar population to their spectra which represents a major observational problem and compromises the reliability of the emission-line intensities. Its proper subtraction however requires the detailed modelling of the stellar population and the disentangling of the contribution by the bulge and by any previous stellar generations in the CNSFR themselves. Almost all these regions show the presence of the CaT lines in the far-red (see Hägele et al. 2007a) some of them with equivalent widths that suggest a certain contribution by red supergiant stars. A detailed study of the ionizing and non-ionizing stellar populations of this region will be presented in a forthcoming paper. In the case of the Balmer lines, the presence of wide wings in their profiles, allows to perform a two-component – emission and absorption – Gaussian fit in order to correct the Balmer emission lines for this effect.

We have derived the characteristics of the observed CNSFR in terms of size, Hα luminosities and ionizing cluster masses. The derived sizes are between 1.5 and 5.7 arcsec which correspond to linear dimensions between 74 and 234 pc. The derived filling factors, between 6×10^{-4} and 1×10^{-3}, are lower than commonly found in giant H II regions ($\sim$0.01). Hα luminosities are larger than the typical ones found for disc H II regions and overlap with those measured in H II galaxies. The region with the largest Hα luminosity is R3+R4 in NGC 3504, for which a value of 2.02×10^{40} is measured. Ionizing cluster masses range between 1.1×10^5 and 4.7×10^6 $M_\odot$ but could be lower by factors between 1.5 and 15 if the contribution by the underlying stellar population is taken into account.

The low excitation of the regions, as evidenced by the weakness of the [O III] λ5007 Å line, precludes the detection and measurement of the auroral [O III] λ4363 Å necessary for the derivation of the electron temperature. Only for one of the regions, the [S III] λ6312 Å line was detected providing, together with the nebular [S III] lines at λλ9069, 9532 Å a value of the electron temperature of $T_e([S\,III]) = 8400^{+4650}_{-1250}$ K. A new method for the derivation of sulphur abundances was developed based on the calibration of the [S III] electron temperature versus the empirical parameter SO_{23} defined as the quotient of the oxygen and sulphur abundance parameters O_{23} and S_{23} and the further assumption that $T([S\,III]) \simeq T([S\,II])$. Then the oxygen abundances and the N/O and S/O ratios can also be derived.

The derived oxygen abundances are comparable to those found in high metallicity disc H II regions from direct measurements of electron temperatures and consistent with solar values within the errors. The region with the highest oxygen abundance is R3+R4 in NGC 3504, $12 + \log(O/H) = 8.85$, about 1.5 solar if the solar oxygen abundance is set at the value derived by Asplund et al. (2005), $12 + \log(O/H)_\odot = 8.66 \pm 0.05$. Region R7 in NGC 3351 has the lowest oxygen abundance of the sample, about 0.6 times solar. In all the observed CNSFR the O/H abundance is dominated by the O^+/H^+ contribution, as is also the case for high metallicity disc H II regions. For our observed regions, however, also the S^+/S^{2+} ratio is larger than one, different from the case of high metallicity disc H II regions for which, in general, the sulphur abundances are dominated by S^{2+}/H^+. The derived N/O ratios are in average larger than those found in high metallicity disc H II regions and they do not seem to follow the trend of N/O versus O/H which marks the secondary behaviour of nitrogen. On the other hand, the S/O ratios span a very narrow range between 0.6 and 0.8 of the solar value.

When compared to high metallicity disc H II regions, CNSFR show values of the O_{23} and the N2 parameters whose distributions are shifted to lower and higher values, respectively, hence, even though their derived oxygen and sulphur abundances are similar, higher values would in principle be obtained for the CNSFR if pure empirical methods were used to estimate abundances. CNSFR also show lower ionization parameters than their disc counterparts, as derived from the [S II]/[S III] ratio. Their ionization structure also seems to be different with CNSFR showing radiation field properties more similar to H II galaxies than to disc high metallicity H II regions. The possible contamination of their spectra from hidden low luminosity AGN and/or shocks, as well as the probable presence of more than one velocity component in the ionized gas corresponding to kinematically distinct systems, should be further investigated.

ACKNOWLEDGMENTS

The WHT is operated in the island of La Palma by the Isaac Newton Group in the Spanish Observatorio del Roque de los Muchachos of the Instituto de Astrofísica de Canarias. We thank the Spanish allocation committee (CAT) for awarding observing time.

This work has been partially supported by DGICYT grant AYA-2004-02860-C03. GH acknowledges support from the Spanish MEC through FPU grant AP2003-1821. AID acknowledges support from the Spanish MEC through a sabbatical grant PR2006-0049. Also, partial support from the Comunidad de Madrid under grant S-0505/ESP/000237 (ASTROCAM) is acknowledged. Support from the Mexican Research Council (CONACYT) through grant 49942 is acknowledged by ET. We thank the hospitality of the Institute of Astronomy, Cambridge, where most of this paper was written.

We would like to thank Mike Beasley for providing the digital spectrum of the M31 cluster, Roberto Cid Fernandes for very helpful discussions concerning subtraction procedures of the underlying absorptions and Roberto Terlevich for a careful reading of this manuscript. We also thank an anonymous referee for a very careful review of this work which leads to the improvement of the paper.

This work is dedicated to the memory of Bernard Pagel who was always a source of inspiration and stimuli for us and with whom we discussed many of the matters addressed in this paper over the last twenty years or so.

REFERENCES

Alloin D., Nieto J.-L., 1982, A&AS, 50, 491
Alloin D., Collin-Souffrin S., Joly M., Vigroux L., 1979, A&A, 78, 200
Alonso-Herrero A., Ryder S. D., Knapen J. H., 2001, MNRAS, 322, 757
Asplund M., Grevesse N., Sauval A. J., 2005, in Barnes T. G., III, Bash F. N., eds, ASP Conf. Ser. Vol. 336, Cosmic Abundances as Records of Stellar Evolution and Nucleosynthesis. Astron. Soc. Pac., San Francisco, p. 25
Athanassoula E., 1992, MNRAS, 259, 328
Baldwin J. A., Phillips M. M., Terlevich R., 1981, PASP, 93, 5
Balick B., Sneden C., 1976, ApJ, 208, 336
Balzano V. A., 1983, ApJ, 268, 602
Barmby P., Huchra J. P., Brodie J. P., Forbes D. A., Schroder L. L., Grillmair C. J., 2000, AJ, 119, 727
Bottinelli L., Gouguenheim L., Paturel G., de Vaucouleurs G., 1984, A&AS, 56, 381
Bresolin F., Garnett D. R., Kennicutt R. C., Jr, 2004, ApJ, 615, 228
Bresolin F., Schaerer D., González Delgado R. M., Stasińska G., 2005, A&A, 441, 981

Brocklehurst M., 1971, MNRAS, 153, 471
Castellanos M., Díaz A. I., Terlevich E., 2002, MNRAS, 329, 315
Cerviño M., Valls-Gabaud D., Luridiana V., Mas-Hesse J. M., 2002, A&A, 381, 51
Colina L., Garcia Vargas M. L., Mas-Hesse J. M., Alberdi A., Krabbe A., 1997, ApJ, 484, L41
Combes F., Gerin M., 1985, A&A, 150, 327
Denicoló G., Terlevich R., Terlevich E., 2002, MNRAS, 330, 69
de Vaucouleurs G., de Vaucouleurs A., Corwin H. G., Jr, Buta R. J., Paturel G., Fouque P., 1991, Third Reference Catalogue of Bright Galaxies, Vol. 1–3. Springer-Verlag, Berlin
Devereux N. A., 1989, ApJ, 346, 126
Devereux N. A., Kenney J. D., Young J. S., 1992, AJ, 103, 784
Díaz A. I., 1989, in Beckman J. E., Pagel B. E. J., eds, Evolutionary Phenomena in Galaxies. Cambridge Univ. Press, Cambridge, p. 377
Díaz Á. I., 1998, Ap&SS, 263, 143
Díaz A. I., Pérez-Montero E., 2000, MNRAS, 312, 130
Díaz A. I., Pagel B. E. J., Wilson I. R. G., 1985, MNRAS, 212, 737
Díaz A. I., Terlevich E., Pagel B. E. J., Vílchez J. M., Edmunds M. G., 1987, MNRAS, 226, 19
Díaz A. I., Terlevich E., Vílchez J. M., Pagel B. E. J., Edmunds M. G., 1991, MNRAS, 253, 245
Díaz A. I., Castellanos M., Terlevich E., Luisa García-Vargas M., 2000, MNRAS, 318, 462
Elmegreen D. M., Chromey F. R., Santos M., Marshall D., 1997, AJ, 114, 1850
García-Rojas J., 2006, PhD thesis, Universidad de la Laguna
García Vargas M. L., Díaz A. I., 1994, ApJS, 91, 553
Garnett D. R., 1992, AJ, 103, 1330
Garnett D. R., Shields G. A., Skillman E. D., Sagan S. P., Dufour R. J., 1997, ApJ, 489, 63
Gonzalez Delgado R. M., Perez E., 1996, MNRAS, 281, 781
Gonzalez-Delgado R. M. et al., 1994, ApJ, 437, 239
González-Delgado R. M., Pérez E., Díaz A. I., García-Vargas M. L., Terlevich E., Vílchez J. M., 1995, ApJ, 439, 604
Graham J. A. et al., 1997, ApJ, 477, 535
Groves B. A., Heckman T. M., Kauffmann G., 2006, MNRAS, 371, 1559
Hägele G. F., Pérez-Montero E., Díaz Á. I., Terlevich E., Terlevich R., 2006, MNRAS, 372, 293
Hägele G. F., Díaz Á. I., Cardaci M. V., Terlevich E., Terlevich R., 2007a, MNRAS, 378, 163
Hägele G. F., Díaz A. I., Terlevich E., Terlevich R., Pérez-Montero E., Cardac M. V., 2007b, MNRAS, submitted
Hoyos C., Díaz A. I., 2006, MNRAS, 365, 454
Kauffmann G. et al., 2003, MNRAS, 346, 1055
Kenney J. D. P., Wilson C. D., Scoville N. Z., Devereux N. A., Young J. S., 1992, ApJ, 395, L79
Kennicutt R. C., Jr, Keel W. C., Blaha C. A., 1989, AJ, 97, 1022
Kennicutt R. C., Jr, Bresolin F., Garnett D. R., 2003, ApJ, 591, 801
Kewley L. J., Dopita M. A., Sutherland R. S., Heisler C. A., Trevena J., 2001, ApJ, 556, 121
Miller J. S., Mathews W. G., 1972, ApJ, 172, 593
Mollá M., Vílchez J. M., Gavilán M., Díaz A. I., 2006, MNRAS, 372, 1069
Oke J. B., 1990, AJ, 99, 1621
Oke J. B., Gunn J. E., 1983, ApJ, 266, 713
Osterbrock D. E., 1989, Astrophysics of Gaseous Nebulae and Active Galactic Nuclei. University Science Books, Mill Valley, CA, p. 422
Pagel B. E. J., Edmunds M. G., Blackwell D. E., Chun M. S., Smith G., 1979, MNRAS, 189, 95
Pagel B. E. J., Simonson E. A., Terlevich R. J., Edmunds M. G., 1992, MNRAS, 255, 325
Pastoriza M. G., Dottori H. A., Terlevich E., Terlevich R., Díaz A. I., 1993, MNRAS, 260, 177
Pérez-Montero E., Díaz A. I., 2003, MNRAS, 346, 105
Pérez-Montero E., Díaz A. I., 2005, MNRAS, 361, 1063
Pérez-Olea D., 1996, PhD thesis, Universidad Autónoma de Madrid
Phillips M. M., Pagel B. E. J., Edmunds M. G., Díaz A., 1984, MNRAS, 210, 701
Pilyugin L. S., 2007, MNRAS, 375, 685
Pilyugin L. S., Vílchez J. M., Contini T., 2004, A&A, 425, 849
Pilyugin L. S., Thuan T. X., Vílchez J. M., 2006, MNRAS, 367, 1139
Planesas P., Colina L., Perez-Olea D., 1997, A&A, 325, 81
Puxley P. J., Hawarden T. G., Mountain C. M., 1990, ApJ, 364, 77
Sérsic J. L., Pastoriza M., 1967, PASP, 79, 152
Shaw R. A., Dufour R. J., 1995, PASP, 107, 896
Skillman E. D., Kennicutt R. C., Jr, 1993, ApJ, 411, 655
Skillman E. D., Televich R. J., Kennicutt R. C., Jr, Garnett D. R., Terlevich E., 1994, ApJ, 431, 172
Stasińska G., 2006, A&A, 454, L127
Stasińska G., Leitherer C., 1996, ApJS, 107, 661
Tayal S. S., Gupta G. P., 1999, ApJ, 526, 544
Vila-Costas M. B., Edmunds M. G., 1992, MNRAS, 259, 121
Vilchez J. M., Pagel B. E. J., 1988, MNRAS, 231, 257
Vílchez J. M., Pagel B. E. J., Díaz A. I., Terlevich E., Edmunds M. G., 1988, MNRAS, 235, 633
Zaritsky D., Kennicutt R. C., Jr, Huchra J. P., 1994, ApJ, 420, 87

This paper has been typeset from a TEX/LATEX file prepared by the author.